The Astrophysical Journal, 946:61 (24pp), 2023 April 1 https://doi.org/10.3847/1538-4357/acb137

A Spectroscopic Analysis of a Sample of K2 Planet-host Stars: Stellar Parameters, Metallicities and Planetary Radii

V. Loaiza-Tacuri[1], Katia Cunha[1,2,3], Verne V. Smith[3,4], Cintia F. Martinez[5], Luan Ghezzi[6], Simon C. Schuler[7], Johanna Teske[8], and Steve B. Howell[9]

[1] Observatório Nacional, Rua General José Cristino, 77, 20921-400 São Cristóvão, Rio de Janeiro, RJ, Brazil; vtacuri@on.br
[2] Steward Observatory, University of Arizona, 933 North Cherry Avenue, Tucson, AZ, 85721, USA
[3] Institut d'Astrophysique de Paris, UMR 7095 CNRS, Sorbonne Université, 98bis Bd. Arago, 75014 Paris, France
[4] NSF's NOIRLab, 950 North Cherry Avenue, Tucson, AZ, 85719, USA
[5] Instituto de Astronomía y Física del Espacio, Universidad de Buenos Aires, Ciudad Universitaria S/N, Buenos Aires, Argentina
[6] Universidade Federal do Rio de Janeiro, Observatório do Valongo, Ladeira do Pedro Antônio, 43, Rio de Janeiro, RJ 20080-090, Brazil
[7] University of Tampa, 401 W Kennedy Boulevard, Tampa, FL, 33606, USA
[8] Carnegie Earth & Planets Lab, 5241 Broad Branch Road, NW, Washington, DC, 20015, USA
[9] NASA Ames Research Center, Moffett Field, CA, 94035, USA

Received 2022 September 22; revised 2023 January 6; accepted 2023 January 6; published 2023 March 30

Abstract

The physical properties of transiting exoplanets are connected with the physical properties of their host stars. We present a homogeneous spectroscopic analysis based on the spectra of FGK-type stars observed with the Hydra spectrograph on the WIYN telescope. We derived the effective temperatures, surface gravities, and metallicities, for 81 stars observed by K2 and 33 by Kepler 1. We constructed an Fe I and II line list that is adequate for the analysis of $R \sim 18{,}000$ spectra covering 6050–6350 Å and adopted the spectroscopic technique based on equivalent-width measurements. The calculations were done in LTE using Kurucz model atmospheres and the `qoyllur-quipu` (q^2) package. We validated our methodology via an analysis of a benchmark solar twin and solar proxies, which are used as a solar reference. We estimated the effects that including Zeeman-sensitive Fe I lines have on the derived stellar parameters for young and possibly active stars in our sample and found them not to be significant. Stellar masses and radii were derived by combining the stellar parameters with Gaia EDR3 and V magnitudes and isochrones. The measured stellar radii have a 4.2% median internal precision, leading to a median internal uncertainty of 4.4% in the derived planetary radii. With our sample of 83 confirmed planets orbiting K2 host stars, the radius gap near $R_{\rm planet} \sim 1.9\,R_{\oplus}$ is detected, in agreement with previous findings. Relations between the planetary radius, orbital period, and metallicity are explored and these also confirm previous findings for Kepler 1 systems.

Unified Astronomy Thesaurus concepts: Fundamental parameters of stars (555); Spectroscopy (1558); Exoplanet systems (484); F stars (519); G stars (558); K stars (878)

Supporting material: machine-readable tables

1. Introduction

To date, according to the NASA Exoplanet Archive[10] and Exoplanet Catalog,[11] there are more than ∼5000 detected exoplanets orbiting ∼3800 parent stars, with most of these planets (∼3900) discovered via the transit method. This impressive number of planets detected via transits so far, is thanks to the Corot mission (37 planets; Deleuil et al. 2000, 2018), the more recent TESS mission (249 planets; Ricker et al. 2015), and mostly thanks to the Kepler Mission (2708 planets; Borucki et al. 2010; Koch et al. 2010; Borucki 2016), along with the extended K2 mission (537 planets; Howell et al. 2014). The original Kepler mission (Kepler 1; operating between 2009 and 2013) pointed at a single field of view in the constellations of Cygnus and Lyra. For the K2 mission (operating between 2014 and 2018), the Kepler telescope was reoriented to point at different fields along the ecliptic plane for about 80 days each, with a latency period between them as the spacecraft orbited the Sun. One advantage of the change in targeting strategy during the Kepler mission, due to the loss of two of the guidance gyros in the Kepler telescope, is that K2 observed Galactic targets in regions of the disk that Kepler 1 had not reached. It is also relevant to note that K2 targeted a larger and more diverse sample compared to Kepler 1.

Determining stellar atmospheric parameters (effective temperatures, metallicities, and surface gravities) of exoplanet host stars is crucial to exoplanet studies because host-star parameters must be known with precision in order to derive precise fundamental planetary properties. One key stellar parameter that needs to be determined as precisely as possible is the stellar radius, as planetary transits essentially measure the ratio of the planet radius to stellar radius. Using a quantitative high-resolution stellar spectroscopic analysis to derive more precise stellar radii, the California Kepler Survey (CKS; Petigura et al. 2017) made the important discovery of a bimodal distribution in the radii of small planets, where the separation between the peaks falls at $R_{\rm pl} \sim 1.8\,R_{\oplus}$ (see Figure 7 of Fulton et al. 2017). The gap in planet radius (now known as the Fulton gap, or also referred to as the radius valley) represents the

---

[10] https://exoplanetarchive.ipac.caltech.edu/

[11] https://exoplanets.nasa.gov/discovery/exoplanet-catalog/

transition from super-Earths to mini-Neptunes and had been predicted by models (Lopez & Fortney 2013; Owen & Wu 2013; Ginzburg et al. 2018; Gupta & Schlichting 2019). This bimodal distribution has been confirmed independently by other studies that reached high-enough precision in their derived radii to uncover and confirm the radius gap (Berger et al. 2018; Fulton & Petigura 2018; Van Eylen et al. 2018; Martinez et al. 2019). Van Eylen et al. (2018) used asteroseismology for a small sample of host stars (75 host stars and 117 planets) and derived a negative slope for the value of the radius gap versus orbital period, while Martinez et al. (2019), using a precise classical high-resolution spectroscopic analysis, measured a similar slope for the radius gap using the larger CKS sample (1232 host stars and 1633 planets).

According to the two theoretical models that predict the radius gap, core-powered mass loss and mass loss by photoevaporation, there is a variation with stellar mass (Fulton & Petigura 2018). Photoevaporation models predict that the loss of the outer layers of gaseous planets is associated with the radiation (X-rays and EUV) from their host stars (Lopez & Fortney 2013; Owen & Wu 2013), while core-powered mass-loss models predict that the loss of the atmospheric mass of the planet is caused by the energy of the young and hot planetary cores (Ginzburg et al. 2016, 2018; Gupta & Schlichting 2019). In that sense, several studies have shown that there is a dependence of the radius gap on stellar mass (i.e., Fulton & Petigura 2018; Berger et al. 2020a; Cloutier & Menou 2020; Van Eylen et al. 2021). Importantly, Cloutier & Menou (2020) showed that the radius gap persists in low-mass stars ($M_{\rm star} = 0.08$–$0.93\ M_\odot$). However, Petigura et al. (2022) investigated the radius gap and found no evidence that it is a function of the stellar mass of host stars (for $M_{\rm star} = 0.5$–$1.4\ M_\odot$).

Besides stellar radii, the stellar metallicity of host stars is another parameter that is important in studying possible star–planet connections. Several studies have investigated and found the well-known correlation between the occurrence of giant planets and host-star metallicity; the formation of giant planets is favored around stars with larger metal content (e.g., Gonzalez 1997; Santos et al. 2004; Fischer & Valenti 2005; Ghezzi et al. 2010; Sousa et al. 2011; Ghezzi et al. 2018; Adibekyan 2019). This correlation has played an important role in the exoplanet field, especially in planet formation theory (e.g., Ida & Lin 2004a, 2004b, 2005; Nayakshin 2010; Mordasini et al. 2012, 2015; Owen & Murray-Clay 2018; Venturini et al. 2020).

Unlike the well-established planet–metallicity correlation for giant planets, it is still unclear whether smaller planets (planet radius $R_{\rm pl} < 4\,R_\oplus$, or planet mass $M_{\rm pl} < M_{\rm Neptune}$), especially terrestrial planets ($R_{\rm pl} < 1.7 R_\oplus$; Buchhave et al. 2014), also follow a planet–metallicity correlation. Early studies showed that planets with a radius $R_{\rm pl} < 4\,R_\oplus$ display a wide range of metallicities indistinguishable from the distribution of stars without planets (e.g., Buchhave et al. 2012; Everett et al. 2013). Several additional studies have analyzed the small planet–metallicity correlation based on a large sample of transiting exoplanets from the Kepler catalog. These studies used spectroscopic stellar metallicities and concluded that small-rocky planets ($R_{\rm pl} < 1.7\,R_\oplus$) do not show a preference for metal-rich stars (e.g., Sousa et al. 2008; Batalha et al. 2013; Buchhave et al. 2014; Buchhave & Latham 2015; Schuler et al. 2015; Mulders et al. 2016; Petigura et al. 2018a; Narang et al. 2018; Adibekyan 2019), while the occurrence rate of larger transiting planets ($R_{\rm pl} \sim 1.7$–$3.9\,R_\oplus$) show a correlation with metallicity (Buchhave & Latham 2015; Mulders et al. 2016; Narang et al. 2018). But Wang & Fischer (2015) suggested a universality around the planet–metallicity correlation, indicating that not only giant planets ($R_{\rm pl} > 4\,R_\oplus$), but also gas dwarf planets ($R_{\rm pl} \sim 1.7$–$3.9\,R_\oplus$) and terrestrial planets ($<1.7\,R_\oplus$) occur most often in metal-rich stars. Zhu et al. (2016) tried to explain this discrepancy, i.e., if the planet–metallicity correlation is universal or not, by suggesting that it is due to a high rate of planet occurrence and low detection efficiency. Aside from the rate of occurrence, various studies analyzed the relationship between orbital period and metallicity, concluding that small and hot planets (orbital periods of $P \lesssim 10$ days) appear preferentially around metal-rich stars (e.g., Adibekyan et al. 2013; Beauge & Nesvorny 2013; Adibekyan et al. 2015; Dawson et al. 2015; Mulders et al. 2016; Petigura et al. 2018a; Dong et al. 2018; Owen & Murray-Clay 2018; Wilson et al. 2018). Another correlation that has been investigated is the influence of the stellar metallicity on the planetary system architecture (Weiss et al. 2018; Ghezzi et al. 2021).

The studies highlighted above demonstrate that it is important to characterize well exoplanet stellar hosts in terms of their stellar parameters and metallicities. For example, via community effort (ExoPAG; Gaudi 2013),[12] significant progress has been made toward this goal in recent years. We point out, however, that there have been far fewer detailed spectroscopic studies of stars observed in the extended K2 mission when compared to the Kepler 1 mission, with most of the K2 star compilations of results so far being based on photometric and asteroseismic analyses, or trigonometric methods (e.g., Boyajian et al. 2013; Vanderburg et al. 2016; Huber et al. 2017; Berger et al. 2020b). Together with precise EDR3 Gaia (Gaia Collaboration et al. 2021) parallaxes, deriving precise stellar parameters for K2 stars via high-resolution spectra can be considered a necessity for the community. This study focuses on the homogeneous spectroscopic analysis of a sample of K2 stars using optical spectra obtained with the Hydra Spectrograph on the WIYN 3.5 m telescope and measurements of selected Fe I and Fe II lines to derive fundamental stellar properties, such as $T_{\rm eff}$, log g, [Fe/H], mass, and radius. Most of the target K2 stars in this study have confirmed planets and their stellar radii are used to compute precise radii for K2 planets.

This paper is organized as follows. In Section 2, we describe the observations and data reduction. In Section 3, we discuss the methodology employed in the derivation of the stellar parameters, effective temperatures, surface gravities, metallicities, stellar masses, and radii, along with planetary radii. In Section 4, our results are presented. Finally, discussions and conclusions are presented in Sections 5 and 6, respectively.

2. Observations

The spectra analyzed in this study were obtained in several observing runs targeting stars from the Ecliptic Plane Input Catalog (EPIC) for the K2 mission and, as a lower priority, Kepler objects of interest (KOI) from the Kepler 1 mission. The observing runs took place between 2015 and 2019 using the Hydra multifiber spectrograph ($R \sim 18{,}500$) mounted on the WIYN 3.5 m telescope at Kitt Peak.[13] Most of the observed stars are from the K2 mission.

---

[12] https://exoplanets.nasa.gov/exep/exopag/overview/

[13] The WIYN Observatory is a joint facility of the University of Wisconsin–Madison, Indiana University, NSF's NOIRLab, the Pennsylvania State University, Purdue University, University of California, Irvine, and the University of Missouri.

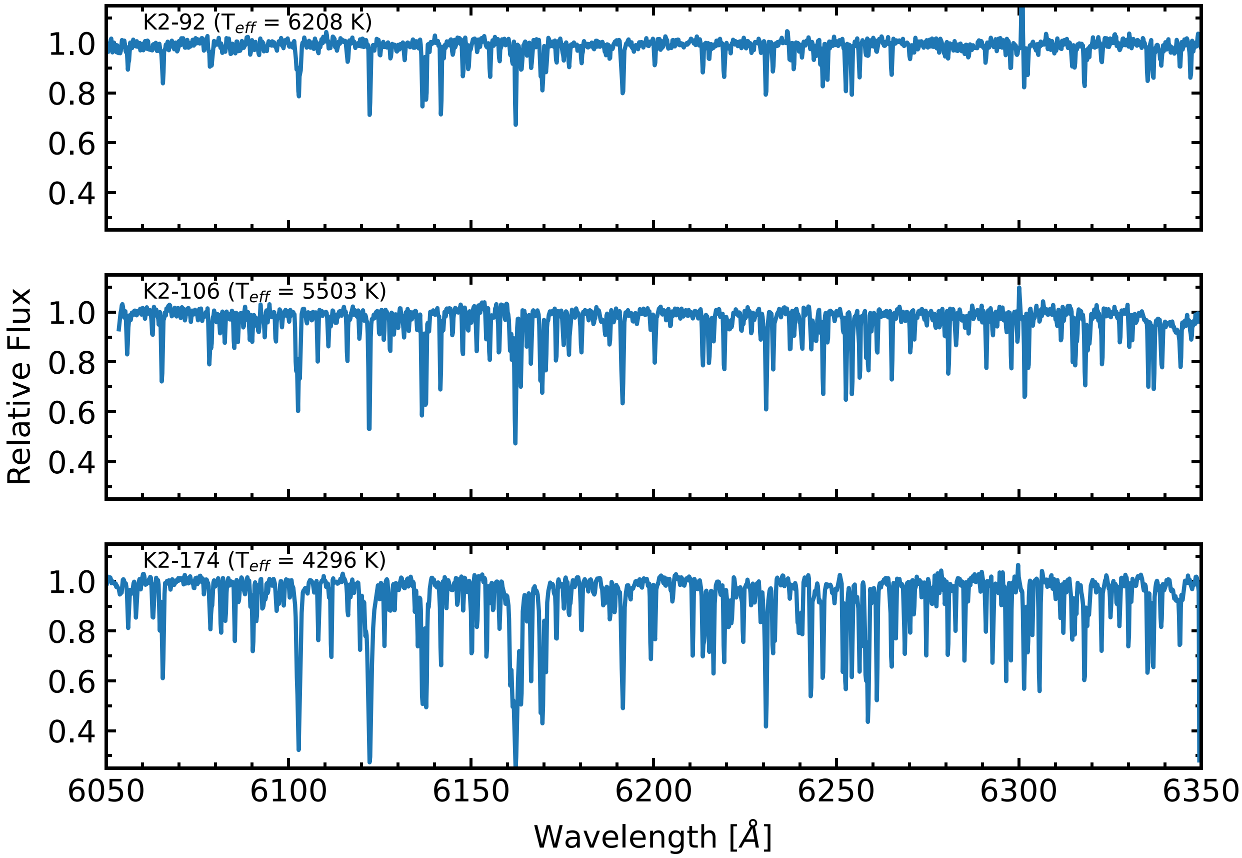

Figure 1. Examples of reduced Hydra spectra; the top, middle, and lower panels correspond to the target stars K2-92 ($T_{\rm eff} = 6208$K; F dwarf), K2-106 ($T_{\rm eff} = 5503$K; G dwarf), and K2-174 ($T_{\rm eff} = 4296$K; K dwarf), respectively. The increasing spectral-line absorption from spectral type F to G to K is clear, which arise from both a larger number of lines plus increasing line absorption.

The Hydra spectra were reduced using routines in IRAF.[14] - Briefly, we trimmed and overscan-subtracted the individual frames. The bias frames were combined into a master bias and then this was subtracted from the rest of the images. Cosmic rays from object frames were removed using L. A. Cosmic, an IRAF script developed by van Dokkum (2001). After aperture extraction, the 1D spectra were flat fielded and wavelength calibrated. Finally, to remove the telluric lines between 6270 and 6300 Å we used the spectrum of a rapidly rotating B-type star. The continuum normalization of all spectra was done with the IRAF task continuum and a spline fit. Figure 1 displays the continuum-normalized spectra showing the entire wavelength range (6050 to 6350 Å) covered by the analyzed Hydra spectra. The three stars presented in the different panels of the figure were selected to showcase the change in spectral features due to different effective temperatures. The top panel shows a hotter star with $T_{\rm eff} = 6208$ K (K2-92), the middle panel a star with $T_{\rm eff} = 5503$ K (K2-106), and the bottom panel a cooler star with $T_{\rm eff} = 4296$ K (K2-174). The effective temperatures in the panels are those from this study.

The sample studied here contains 115 stars and the targets were selected based on observability, and with an emphasis on G and K spectral types (Section 5). Our prime program was to target K2 stars but due to observing constraints Kepler 1 targets were also observed. The total number of K2 stars analyzed is 81 (69 stars with confirmed planets and 12 stars with candidate planets) and it includes stars from campaigns C0, C1, C3−C6, C8, and C10 (some stars from C5 were also observed in C16 and C18). Our sample includes 33 stars identified as Kepler, KOIs, or KIC, plus two asteroids observed as solar proxies (Astraea and Phartenopen). We also observed a solar twin (HIP 81512), which was analyzed previously by Ramirez et al. (2009, 2013), as a comparison star. The quality of the spectra in this analysis are good and suitable for a precise spectroscopic analysis with most of the spectra having a signal-to-noise ratio (S/N) of ∼100, while about 10% of the spectra have $50 < \mathrm{S/N} < 100$. The S/N were estimated in spectral regions between ∼6068–6075 Å.

In our sample there are seven stars that have been flagged as eclipsing binaries: KOI-6 by Slawson et al. (2011), EPIC 202126847 by LaCourse et al. (2015), EPIC 210754505 by Barros et al. (2016), EPIC 201569483, EPIC 202071289, EPIC 202086968, and K2-10 by Armstrong et al. (2015). In order to evaluate if there is evidence of a companion star in the observed spectra, all seven stars have been inspected carefully, finding no trace of contamination by a second set of spectral lines from a companion, although some small level (∼1%–2%) effect may still be present. In any case, these stars do not enter into the calculation of any planetary radii, except for K2-10. We note, that the exoplanet archive classifies K2-10 as a confirmed planet-host based on the following studies: Kruse et al. (2019), Van Eylen et al. (2016), Vanderburg et al. (2016), Montet et al. (2015), Barros et al. (2016), and Crossfield et al. (2016). We also note that Lester et al. (2021) and Howell et al. (2021), have shown that in binary systems,

---

[14] IRAF is distributed by the National Optical Astronomy Observatory, which is operated by the Association of Universities for Research in Astronomy, Inc., under a cooperative agreement with the National Science Foundation.

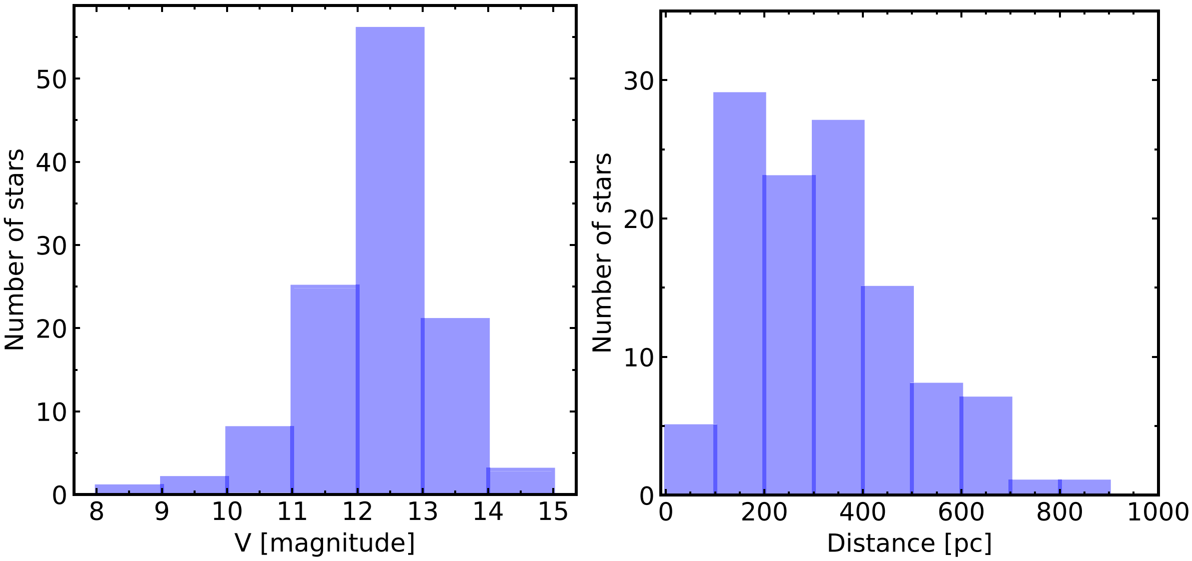

Figure 2. The distributions of V magnitudes and distances for the sample stars. Distances were taken from Bailer-Jones et al. (2021), using Gaia EDR3 data, with V magnitudes from the NASA Exoplanet Archive.

Table 1
Main Sample Data

ID	Host Name	UT Date	R.A.	Decl.	V (mag)	Exposure (s)	S/N
EPIC201403446	K2-46	2018 Mar 30	11:37:03.92	−00:54:26.10	12.03	2 × 1800	135
EPIC211355342	K2-181	2018 Mar 30	08:30:12.97	10:54:37.04	12.75	3 × 1800	95
EPIC201736247	K2-15	2016 Mar 16	11:52:26.59	04:15:17.10	14.76	2 × 1800	50
…	…	…	…	…	…	…	

(This table is available in its entirety in machine-readable form.)

smaller planets ($R < 2\,R_{\oplus}$) are not detected as the companion "third-light" would fill in their shallow transit.

In addition to systems that have been identified as eclipsing binaries, eight of the Kepler 1 targets here have been found to have nearby companion stars lying less than 1″ away from the primary star. These stars were taken from Furlan et al. (2017) and are: Kepler-132, KOI-1119, Kepler-1040, Kepler-396, Kepler-1339, Kepler-1505, Kepler-1525, and Kepler-1542. The reported separations range from 0.04″ to 0.88″ and in all cases the companion was fainter than the primary. Using values of Δmagnitudes from Furlan et al. (2017) (mostly ΔK-magnitudes), convolved with a 1″ seeing-disk, it is found that the expected contaminations, in all but one target, are small, with estimated flux contaminations of 0.3%–4.4%. The one primary target with a very close (0.″04) companion having nearly the same brightness is Kepler-1505 (Δmagnitude$(562) = 0.00 \pm 0.15$ and Δmagnitude$(880) = 0.16 \pm 0.15$; Furlan et al. 2017) and, at an estimated distance of 488 pc, the projected sky separation would be ∼20 au. Composite spectra that are not properly modeled can lead to uncertainties in the derived stellar parameters (Furlan & Howell 2017). Due to likely significant contamination of the spectrum of Kepler-1505 from its companion, this star was removed from the sample.

The main observational data, such as identifiers, observation dates, positions, V magnitudes (taken from NASA Exoplanet Archive), exposure time per spectrum, and S/Ns of the reduced spectra are presented in Table 1.

Histograms with V magnitudes and distances for our sample are presented in the left and right panels of Figure 2, respectively. The V-magnitude distribution of the observed targets peaks at $V \sim 12.5$ and goes as faint as $V \sim 15$. The target distances shown in the right panel of Figure 2 were estimated by Bailer-Jones et al. (2021) using the parallaxes and G-magnitude and $G_{\rm BP}$–$G_{\rm RP}$ color from Gaia EDR3. The studied sample is dominated by stars whose distances are less than 600 pc, with the distance distribution having a peak at approximately 300 pc.

3. Analysis

3.1. Spectroscopic Stellar Parameters

The spectroscopic analysis employed here assumes local thermodynamic equilibrium (LTE) and uses 1D plane parallel model atmospheres from the Kurucz ATLAS9 ODFNEW grid (Castelli & Kurucz 2003). Stellar spectroscopic parameters, namely the effective temperature ($T_{\rm eff}$), surface gravity (log g), iron abundance (A(Fe)[15]), and microturbulent velocity (ξ) were derived using a standard spectroscopic methodology which is based on measurements of the equivalent widths (EWs) of selected iron lines (Fe I and Fe II lines).

The adopted line list in this study was taken from Ghezzi et al. (2018), Meléndez et al. (2014), and Friel et al. (2003) and within the Hydra spectral window, a list of 25 Fe I lines and 5 Fe II lines was selected for analysis. The EWs of the selected

---

[15] $A(X) = \log(N(X)/N(H)) + 12.0$.

Table 2
Iron Line List

λ (Å)	Species	χ (eV)	log *gf*	References
6056.004	Fe I	4.733	−0.558	G18
6085.257	Fe I	2.759	−2.908	G18
6094.374	Fe I	4.650	−1.650	F03
6096.664	Fe I	3.984	−1.861	G18
6098.243	Fe I	4.559	−1.825	G18
6100.271	Fe I	4.559	−2.201	K14
6127.906	Fe I	4.143	−1.503	G18
6151.617	Fe I	2.176	−3.357	G18
6157.727	Fe I	4.076	−1.257	G18
6165.359	Fe I	4.143	−1.487	G18
6173.334	Fe I	2.223	−2.938	G18
6187.989	Fe I	3.943	−1.724	G18
6200.312	Fe I	2.608	−2.457	G18
6213.429	Fe I	2.223	−2.650	G18
6219.280	Fe I	2.198	−2.549	G18
6226.734	Fe I	3.884	−2.143	G18
6229.230	Fe I	2.850	−3.040	F03
6232.640	Fe I	3.654	−1.232	G18
6252.555	Fe I	2.404	−1.687	M14
6265.132	Fe I	2.176	−2.633	G18
6270.225	Fe I	2.858	−2.540	M14
6322.690	Fe I	2.590	−2.250	F03
6335.329	Fe I	2.198	−2.423	G18
6336.824	Fe I	3.686	−0.856	BK94
6344.150	Fe I	2.430	−2.970	F03
6084.102	Fe II	3.199	−3.840	G18
6113.319	Fe II	3.221	−4.155	G18
6149.246	Fe II	3.889	−2.789	G18
6238.386	Fe II	3.889	−2.634	G18
6247.557	Fe II	3.892	−2.427	G18

Note. The sources for the log *gf* values are given in the last column. G18: Ghezzi et al. (2018), M14: Meléndez et al. (2014), F03: Friel et al. (2003), K14: Kurucz (2014), and BK94: Bard & Kock (1994).

lines were measured using the ARES code v2 (Sousa et al. 2015). In Table 2 we present the Fe I and Fe II lines, the excitation potential energies χ, the oscillator strengths (log *gf*), and the respective references for the latter.

Three conditions were required for obtaining a consistent solution for $T_{\rm eff}$, log g, and ξ for the stars. To obtain $T_{\rm eff}$, the excitation equilibrium was required, or, removing trends between A(Fe I) and the excitation potential (χ), of the lines. To obtain log g, the ionization equilibrium was required, or, requiring that the average abundances of the Fe I (A(Fe I)) and Fe II (A(Fe II)) lines are equal. By minimizing the slope (<0.005) of the relationship between A(Fe I) and the logarithm of the reduced EWs (log(EW/λ)), the microturbulent velocity, ξ, is obtained. Finally, the iron abundances were consistent with the input model metallicities.

In order to analyze a relatively large number of stars in a homogeneous and efficient way, we used the automated stellar parameter and metallicity code named `qoyllur-quipu` (or q^2).[16] This is a Python code developed by Ramirez et al. (2014). Briefly, q^2 uses an input iron line list and measured EWs, along with the 2019 version of the abundance analysis code MOOG (Sneden 1973), to compute the iron abundances, effective temperatures, and surface gravities. The iterative process starts by interpolating a model atmosphere calculated assuming given values for $T_{\rm eff}$, log g, and metallicity and then the values of $T_{\rm eff}$, log g, and A(Fe) are increased or decreased iteratively to minimize the slopes of the relationships, and until obtaining a final adjusted value for the spectroscopic parameters of each star. Figure 3 shows an example of the iterated solution for the sample star HIP 81512, obtained for $T_{\rm eff} = 5752$ K, log $g = 4.34$, and $\xi = 1.06$ km s^{-1}, with the mean metallictity for this star represented by the solid blue line.

Table 3 presents the derived effective temperatures, surface gravities, metallicities, and microturbulent velocities for all stars in our sample, as well as the stellar radii and masses (see Section 3.3). We note that for a few stars having no measurable Fe II lines in their spectra, or having only one measurable Fe II line with a large uncertainty in the EW, the asteroseismic log g, if available, was adopted and used in the derivation of the effective temperature and microturbulence from the Fe I lines. Alternatively, when an asteroseismic log g was also not available, the Fe I lines were used to estimate the parameters by varying log g in steps of 0.05 dex and finding the log g value that produced the most consistent solution in terms of the scatter in the Fe abundances from the individual lines.

3.2. Solar Proxies and a Solar Twin as Benchmarks

As benchmarks to our methodology and analysis techniques, we also analyzed solar-proxy spectra obtained with the Hydra spectrograph for reflected solar light from two asteroids, Astraea and Parthenope, as well as the well-studied solar twin HIP 81512 as a benchmark. Results are presented in Table 4. The parameters and metallicities obtained for the solar-proxy Astraea ($T_{\rm eff} = 5778$ K, log $g = 4.34$, A(Fe) = 7.51, and $\xi = 1.16$ km s^{-1}) and for Parthenope ($T_{\rm eff} = 5770$ K, log $g = 4.40$, A(Fe) = 7.54, and $\xi = 1.06$ km s^{-1}) are in excellent agreement with the solar parameters, indicating that our methodology does not harbor strong biases for solar-type stars. We note, however, that the mean metallicity for the solar proxies of A(Fe) =7.52 is slightly more metal-rich than the Asplund et al. (2021) ($A({\rm Fe})_\odot = 7.46$) scale, although it is in good agreement with the Magg et al. (2022) ($A({\rm Fe})_\odot = 7.50$) scale. We also note excellent agreement with the stellar parameters derived in the high-precision analysis of the solar twin HIP 81512 by Ramirez et al. (2009) and Ramirez et al. (2013); the latter studies are based on the analysis of high-resolution spectra ($R = \lambda/\Delta\lambda \simeq 60,\ 000$) obtained with the Robert G. Tull coudé spectrograph on the 2.7 m Harlan J. Smith telescope and measurements of 128 Fe I and 16 Fe II lines, obtaining $T_{\rm eff} = 5755 \pm 32$ K, log $g = 4.43 \pm 0.04$ dex, and A(Fe) =7.40 ± 0.04 dex. These comparisons with benchmark spectra can serve as validations for the technique adopted in this study for the analysis of Hydra spectra covering 6050 −6350 Å and the Fe I/Fe II line list from Table 2.

3.3. Stellar Masses and Radii and Planetary Radii

Fundamental stellar properties, such as stellar radius, age, or mass, can be estimated by comparing the positions of stars in a color–magnitude diagram with theoretical isochrones. Gaia DR3 (Gaia Collaboration et al. 2021) currently provides high-precision parallaxes that can be used to determine the absolute magnitudes of large numbers of stars.

Different codes that are available to the community, such as `PARAM` (Girardi et al. 2000; da Silva et al. 2006;

---

[16] https://github.com/astroChasqui/q2

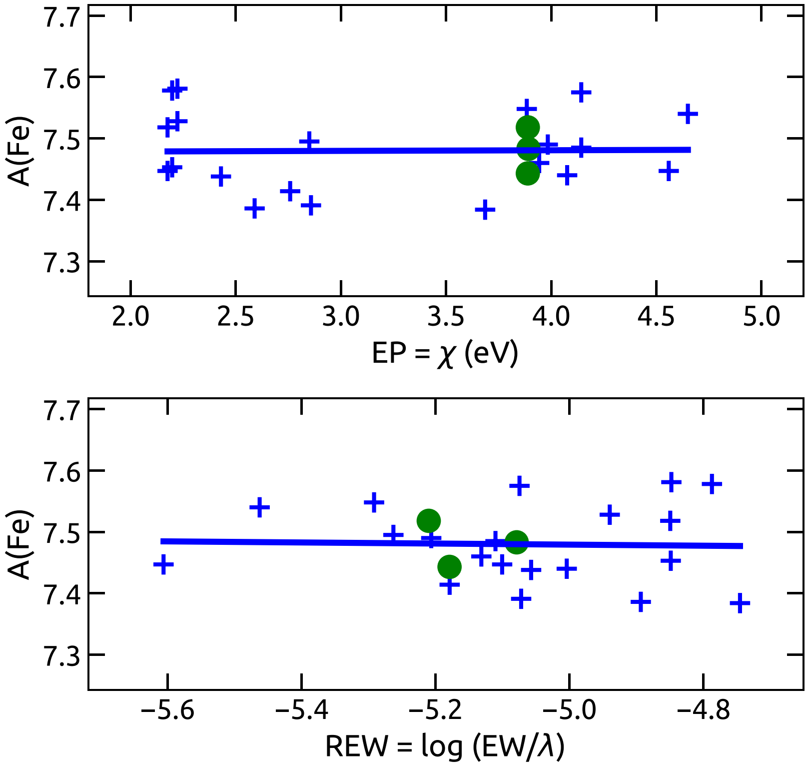

Figure 3. An example of the applied methodology to the solar twin HIP 81512. The top panel shows the iron abundance of the Fe I lines (blue crosses) as a function of excitation potential (χ), which defines the effective temperature of the star. The Fe II transitions are shown as green circles. The bottom panel illustrates the Fe I abundance as a function of the reduced EW (REW) of the Fe lines, which defines the microturbulent velocity parameter.

Rodrigues et al. 2014, 2017), or `isochrones` (Morton 2015), have been developed as interfaces to find best fits to various isochrones, such as MESA Isochrones & Stellar Tracks (MIST; Choi et al. 2016; Dotter 2016), and several works have adopted similar methodologies to obtain stellar masses and radii (e.g., Johnson et al. 2017; Mayo et al. 2018; Wittenmyer et al. 2020).

In this work, stellar masses and radii were computed using the isochrone method via the q^2 code (`qoyllur-quipu`; Ramirez et al. 2014), which determines stellar mass, age, luminosity, and radius, using a grid of Yonsei–Yale isochrones (Yi et al. 2001). Briefly, to determine which isochrones best represent a particular set of observed stellar parameters (spectroscopic $T_{\rm eff}$ and [Fe/H] from this work, along with the M_V absolute magnitude derived from the parallax), probability distributions of those parameters are determined and matched to the isochrones, assuming that the errors in the observed stellar parameters ($\delta\ T_{\rm eff}$, δM_V, and δ [Fe/H]) have Gaussian probability distributions. For more details see Ramirez et al. (2013) and Ramirez et al. (2014). Isochrone-derived masses and radii of the sample stars are shown in Table 3. For five stars, instead of using M_V, we used the log g values to compute the stellar radii and the latter are flagged with an "a" in Table 3. In particular, we opted for using log g when there was a range of V magnitudes reported for a star, which was the case, for example, for two of the eclipsing binaries in our sample. We note that the stellar masses in these cases were estimated in the same way as the other stars using Y^2 isochrones.

Planetary radii were then obtained using the derived stellar radii and the value of the transit depth (ΔF), which is the fraction of stellar flux lost at the minimum of the planetary transit, given by the equation from Seager & Mallen-Ornelas (2003):

$$R_{\rm pl} = 109.1979 \times \sqrt{\Delta F \times 10^{-6}} \times R_{\rm star}, \tag{1}$$

where the radius of the planet is in Earth radii.

We note that in this study, only values of ΔF from confirmed planets were used; we did not consider planets classified as planet candidates and false positives (according to the Kepler 1 and K2 notes in the NASA Exoplanet Archive). Most of the planetary transit depths of the K2 stars were from Kruse et al. (2019) (for 66 confirmed planets); for planets not cataloged by Kruse et al. (2019) we used values from Vanderburg et al. (2016), Pope et al. (2016), Barros et al. (2016), Rizzuto et al. (2017), and Livingston et al. (2018). We note that for K2-100 we noticed that the ΔF from Kruse et al. (2019) was discrepant when compared to other literature sources (e.g., Livingston et al. 2018; Stefansson et al. 2018; Mann et al. 2017; Libralato et al. 2016; Pope et al. 2016) and in this study we adopted the transit depth from Livingston et al. (2018). The transit depth of the planets of Kepler 1 stars were from Thompson et al. (2018) (for 56 confirmed planets). The ΔF values are provided in the Table 6.

3.4. Uncertainties in the Derived Parameters

The formal errors adopted for the stellar parameters $T_{\rm eff}$, log g, and ξ were computed using q^2, which follows the error analysis discussed by Epstein et al. (2010) and Bensby et al. (2014). Errors in the iron abundances, A(Fe I) and A(Fe II), were obtained by combining errors estimated from the EW measurements with the stellar parameter uncertainties. The

Table 3
Stellar Parameters, Radii, and Masses

ID	T_{eff} (K)	$\delta\ T_{\mathrm{eff}}$ (K)	log g (dex)	δlog g (dex)	A(Fe) (dex)	δA(Fe) (dex)	ξ (km s^{-1})	$\delta\ \xi$ (km s^{-1})	R_{star} ($R_\odot$)	$\delta\ R_{\mathrm{star}}$ ($R_\odot$)	M_{star} ($M_\odot$)	$\delta\ M_{\mathrm{star}}$ ($M_\odot$)
EPIC 201166680	6051	289	4.01	0.49	7.39	0.11	1.45	0.37	1.45	0.16	1.09	0.06
EPIC 201211526	5717	176	4.13	0.39	7.21	0.08	1.07	0.17	0.92	0.03	0.89	0.04
EPIC 201257461	4945	160	2.95	0.82	7.41	0.11	1.67	0.18	5.48	0.40	1.25	0.22
…	…	…	…	…	…	…	…	…	…	…	…	…

Note. (*) Asteroseismic log g; (**) no measurable Fe II lines; (a) R_{star} computed using log g values. This table is published in its entirety in the machine-readable format. A portion is shown here for guidance regarding its form and content.

(This table is available in its entirety in machine-readable form.)

Table 4
Stellar Parameters of the Solar Proxies

ID	T_{eff} (K)	log g (dex)	A(Fe) (dex)	ξ (km s^{-1})
Astraea	5778 ± 160	4.34 ± 0.33	7.51 ± 0.09	1.16 ± 0.14
Parthenope	5770 ± 158	4.40 ± 0.36	7.54 ± 0.09	1.06 ± 0.24
HIP 81512	5752 ± 113	4.34 ± 0.33	7.48 ± 0.07	1.06 ± 0.10

Note. $A(\mathrm{Fe})_\odot = 7.46 \pm 0.04$ (Asplund et al. 2021); $A(\mathrm{Fe})_\odot = 7.52 \pm 0.06$ dex (Magg et al. 2022).

Table 5
Error Budget

Parameter	Median Uncertainty
T_{eff}	154 K
log g	0.36 dex
A(Fe)	0.09 dex
V	0.07 mag
plx	0.02 mas
M_{star}	0.04 $M_\odot$
R_{star}	4.15 %
ΔF	3.35 %
R_{pl}	4.44 %

individual errors of these parameters are presented in Tables 3 and 4.

The median errors in the stellar parameters derived in this study are reported in Table 5: $\delta T_{\mathrm{eff}} = 154$ K, $\delta \log g = 0.36$ dex, $\delta A(\mathrm{Fe}) = 0.09$ dex, and $\delta\xi = 0.24$ km s^{-1}. We note that these are somewhat larger than the typical values from analyses of high-resolution spectra ($R \sim 60{,}000$) in the literature (e.g., Ramirez et al. 2014; Martinez et al. 2019; Ghezzi et al. 2021). Larger errors here are to be expected given that the Hydra spectra have lower resolution ($R \sim 18{,}500$) and smaller wavelength coverage, which results in having a smaller number measurable Fe I lines (25) and Fe II lines (5).

Since the stellar masses and radii and planetary radii of our sample were derived from other parameters, we considered the individual contributions of the errors in each one of the parameters to estimate the error budget (similar to the discussions by Fulton & Petigura 2018; Martinez et al. 2019). The internal precisions (median errors) in the derived effective temperatures and metallicities were discussed above. The error in the V magnitude contributes ∼1% to the stellar radius error, when taking 0.07 mag to be the median error in V magnitude for our stars. The contribution due to errors in the parallaxes corresponds to a median error of 0.02 mas and represents a 0.45% error in the stellar mass and radius.

The stellar radii uncertainty and the transit depth (ΔF) errors have a direct impact on the determination of planetary radii errors. The median internal uncertainty in our derived stellar radii distribution is 4.2%; we adopted the transit depth values ΔF and respective errors from Kruse et al. (2019) and Thompson et al. (2018), which, for the planets in our sample, result in a 3.4% internal precision in ΔF. Finally, these uncertainties lead to a 4.4% internal precision for the R_{pl} error budget. A summary of the contributions to the error budgets in the R_{star} and R_{pl} determinations is presented in Table 5. To assess possible differences in the choice of isochrones we adopted the Darmouth isochrones instead of the Yonsei–Yale ones and found no signicant differences in the derived stellar radii and masses. As an example, for the star Kepler-62 we find $R_{\mathrm{star}} = 0.659 \pm 0.018\ R_\odot$ and $M_{\mathrm{star}} = 0.711 \pm 0.024\ M_\odot$ (using Dartmouth isochrones), while the result in this study is the same but just with a slightly higher uncertainty in the mass: $R_{\mathrm{star}} = 0.659 \pm 0.018\ R_\odot$ and $M_{\mathrm{star}} = 0.711 \pm 0.026\ M_\odot$ (using Yonsei–Yale isochrones).

3.5. Possible Impact of Magnetic Activity on Stellar Parameter Determination

In addition to the various sources of uncertainty discussed in the previous subsection, stellar magnetic activity can also affect the determinations of T_{eff}, ξ, and [Fe/H], as shown by Flores et al. (2016), Yana Galarza et al. (2019), and Spina et al.(2020).

Three stars in our sample had activity indices reported by Brown et al. (2022), who compiled a database of chromospheric activity measurements and surface-averaged large-scale magnetic-field measurements for a sample of FGK main-sequence stars. These stars are K2-229, EPIC 202089657, and Kepler-409, with log $R'_{\mathrm{HK}} = -4.73$, -4.75, and -4.82, respectively, keeping in mind that the Sun has a value of log $R'_{\mathrm{HK}} = -5.02$, which varies by about ±0.01 dex over the Solar activity cycle (Lorenzo-Oliveira et al. 2018).

Stellar magnetic activity effects have been quantified by Spina et al. (2020) via the log R_{HK} index, based on a stellar parameter analysis that relies on relations between the Fe I excitation equilibria and the Fe I reduced EWs (EW/λ), both as functions of the Fe I abundance, in addition to the ionization balance of Fe I and Fe II. These constraints provide the values of T_{eff}, log g, ξ, and [Fe/H], and this is the technique used in our study. The impact that stellar activity has on the derivations of the specific stellar parameters using Fe I and Fe II lines is found to be the greatest for T_{eff}, ξ, and [Fe/H], with almost no effect on log g (as illustrated in Figure 3 of Spina et al. 2020). In rough numbers (from Figure 4 of Spina et al. 2020), $R_{\mathrm{HK}} \sim -4.25$ leads to a lower value of T_{eff} by ∼100 K, while log

$R_{\rm HK} \sim -4.40$ causes a metallicity change of [Fe/H] = −0.05, and a value of log $R_{\rm HK} \sim -4.35$ would lead to a derived microturbulent velocity that is too large by ∼0.3 km $\rm s^{-1}$. A much lower activity level of log $R_{\rm HK} \sim -4.7$–4.8, as measured, for example, for the three target stars mentioned above, would cause an unmeasurable change in the effective temperature, a metallicity change of −0.02 dex, and would lead to a microturbulent velocity change of ∼0.05 km $\rm s^{-1}$. All of these variations are well within the uncertainties in our analysis. These are also in line with the results of Lorenzo-Oliveira et al. (2018) who, for the young solar twin HIP 36515 (log $R_{\rm HK} \sim -4.70$), the stellar parameters derived over its six year activity cycle find a scatter in $T_{\rm eff}$ of ±10 K, ±0.01 in [Fe/H], and ±0.07 km $\rm s^{-1}$ in microturbulent velocity. It is possible, however, that other stars in our sample may have higher levels of activity, although such high activity levels would suggest ages <1 Gyr (Lorenzo-Oliveira et al. 2018) or that the stars are members of close binary systems (Oláh 2007).

As part of an analysis of the young active solar twin HIP 36515 (age ∼ 0.4 Gyr), Yana Galarza et al. (2019) established a list of Fe I and Fe II lines that are sensitive to stellar magnetic activity. Among the lines in our line list that were identified as sensitive to magnetic fields are Fe I 6173 Å, 6200 Å, 6213 Å, 6219 Å, 6252 Å, 6265 Å, and 6270 Å (Table 2) and these have both large Landé factors, coupled with large EWs (through a combination of log *gf* values and excitation potentials). None of our Fe II lines were identified as sensitive to stellar magnetic activity.

We investigated the impact that the inclusion of "sensitive" Fe I lines has on the derivation of stellar parameters by removing these sensitive lines and rederiving the parameters for a selected sample of 15 stars. This subsample contains the three stars with measured values of log $R_{\rm HK}$ mentioned above, plus five stars in our sample with approximate ages from q^2 of <4 Gyr (K2-223, K2-44, Kepler-1339, KOI-6, and KOI-293), and two stars (K2-100 and K2-101) which are members of the young (650 ± 70 Myr; Martin et al. 2018) open cluster M 44. We also added the stars K2-186, K2-34, Kepler-139, Kepler-1445, and Kepler-396, as these have measured flares with energies $>10^{34}$ erg along with log $R_{\rm H\alpha} > -4.4$ in Su et al. (2022), who determined the $R_{\rm H\alpha}$ activity index and flare energy using LAMOST spectra and light curves of stars observed by Kepler 1 and K2.

Figure 4 provides comparisons between the stellar parameters derived in this study (without taking into consideration the possible effects of magnetic fields in the measured Fe I lines) and those obtained including only those Fe I lines that were deemed as insensitive to magnetic fields. The median and median absolute deviation (MAD) values of the differences for each stellar parameter are included in each panel of the figure. The upper left panel shows that the differences in the effective temperatures are less than ∼50 K for most stars, with only two stars, K2-44 and Kepler-1445, having larger differences of $\Delta T_{\rm eff}$ ("Non-sensitive"—"This Work") = −112 K and −142 K, respectively. This result suggests that the differences in the effective temperatures are not significant and, in general, fall within the range of our uncertainties (see Table 5). In the case of log *g* (top right panel), all stars have differences less than 0.09 dex, with the exceptions of K2-44 and Kepler-409 having differences of −0.2 and −0.15 dex, respectively. Given the uncertainties in log *g*, all differences are well within the estimated median uncertainty of 0.36 dex. A similar result is found for values of [Fe/H] (lower left panel), as the median uncertainty in [Fe/H] in this study is 0.09 dex (Table 5), with the largest metallicity difference found being −0.118 for Kepler-1445. According to Spina et al. (2020), magnetic activity is expected to result in an increase in microturbulent velocities for log $R_{\rm HK} > -5.0$, or in active young stars (ages < 4–5 Gyr). The median difference found for the microturbulent velocity parameter is −0.01 and the MAD is 0.06 km $\rm s^{-1}$ (Figure 4), indicating that there is no significant evidence that magnetic activity is measurably affecting the microturbulent velocities in this analysis.

In summary, the stellar parameters derived without the use of the magnetically sensitive lines are within the uncertainties when compared to the parameters from this study that include some Fe I lines that are deemed as lines sensitive to the effects of magnetic fields and activity. This result suggests that the final stellar parameters derived for this sample of stars have not been perturbed significantly by strong magnetic activity.

4. Results and Comparisons with the Literature

4.1. Effective Temperatures and Surface Gravities

In general, there are more results available for Kepler 1 mission targets than for K2. Several studies in the literature (Petigura et al. 2017; Brewer & Fischer 2018; Martinez et al. 2019; Ghezzi et al. 2021) analyzed the CKS (Petigura et al. 2017) but used different analysis techniques. The stellar parameters obtained by Petigura et al. (2017) were derived using synthetic spectra and the codes `SpecMatch` and `SME@XSEDE`; Brewer & Fischer (2018) derived the stellar parameters also using spectral synthesis and the Spectroscopy Made Easy (SME; Piskunov & Valenti 2017) code, while Martinez et al. (2019) and Ghezzi et al. (2021) adopted a methodology that was based on the classical spectroscopic EW method and used the code MOOG (Sneden 1973). Concerning results for K2 targets, in particular, Petigura et al. (2018a), using the same methodology of Petigura et al. (2017), analyzed a sample of 141 K2 candidate planet-host stars, while Wittenmyer et al. (2020) analyzed a sample of 129 K2 planet candidate host stars whose spectra were observed by the K2-HERMES program (Wittenmyer et al. 2018; Sharma et al. 2019; Clark et al. 2022) in the Galactic Archeology with HERMES (GALAH; Buder et al. 2021) survey. In addition, results for a large number of both Kepler 1 and K2 targets were obtained by the low-resolution optical spectroscopic LAMOST survey (Cui et al. 2012; Zong et al. 2018), as well as the high-resolution spectroscopic near-infrared APOGEE survey (Majewski et al. 2017; see also Wilson et al. 2018).

Comparisons of our $T_{\rm eff}$ values with those from the studies mentioned above are shown in the different panels of Figure 5; for each case, the median differences "Other Work–This Work" are given in the top left of each panel, along with the corresponding MADs; in all panels the gray diamonds correspond to Kepler 1 stars, while the blue circles correspond to K2 stars. From the medians and MADs in Figure 5 we can conclude that there is overall good agreement between our effective temperatures and those from the APOGEE and LAMOST surveys, as well as those available from the literature. The mean of the median differences is small, $\Delta T_{\rm eff} \sim -45$ K and the MADs are all below 70 K, except for the comparison with the GALAH results, where MAD = 119 K (Wittenmyer et al. 2020) and

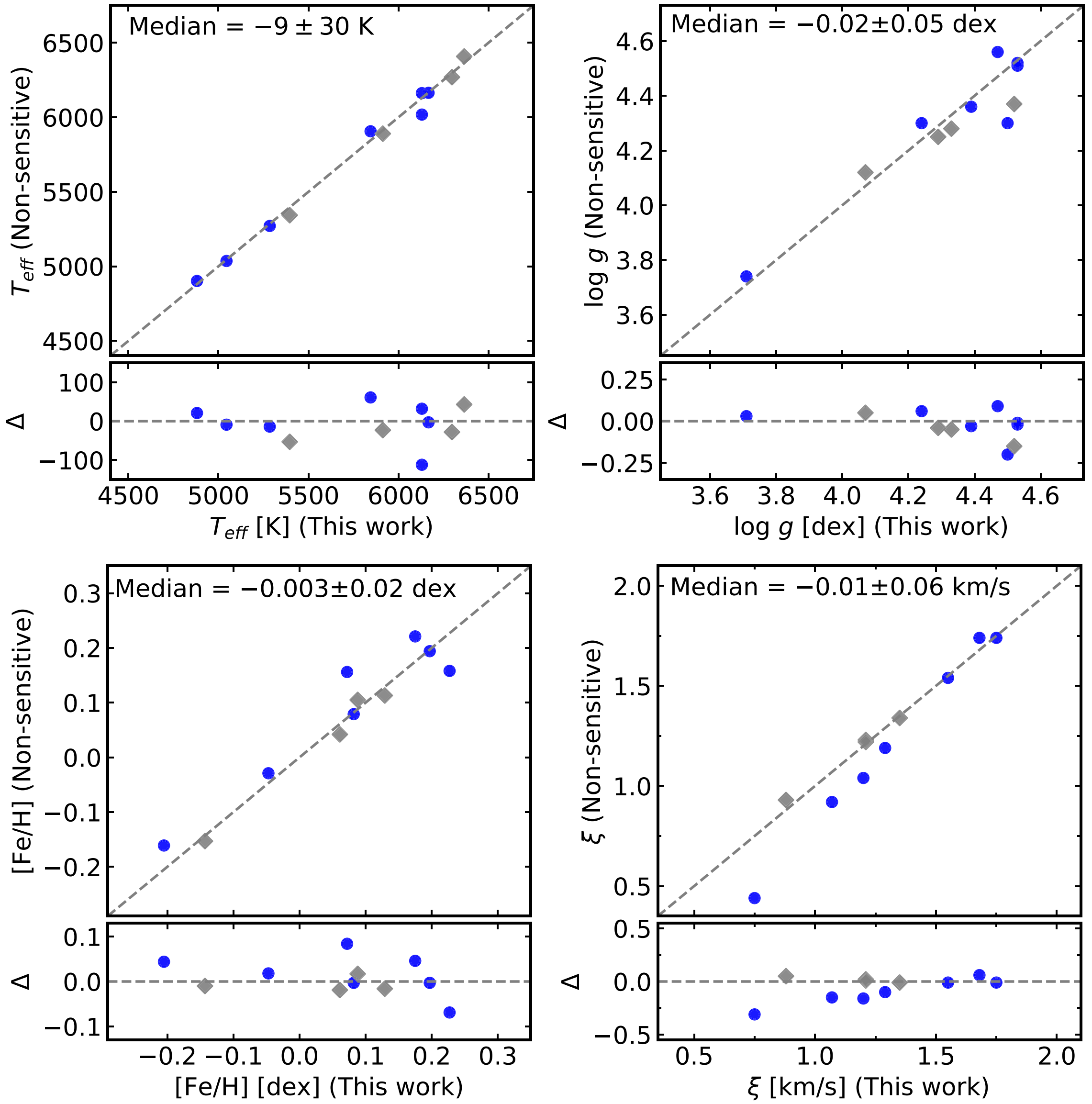

Figure 4. Comparison between the effective temperatures, surface gravities, metallicities, and microturbulent velocities derived in this work with stellar parameters that were rederived using only the subset of the Fe I lines that are deemed as insensitive to the effects of stellar activity ("Non-sensitive"). The bottom panels present the difference, Δ, between the stellar parameters for "Non-sensitive—This work." The blue circles represent K2 stars and gray diamonds Kepler 1 stars. The selected targets include host stars that exhibit flare activity (flares with energies $> 10^{34}$ erg) along with log $R_{\mathrm{H}\alpha} > -4.4$, three stars with a measured chromospheric Ca II index of log R_{HK} ∼−4.7–4.8, five stars that have estimated ages <4 Gyr, and two stars that are members of the young open cluster M 44.

114 K (GALAH). Overall our T_{eff} scale is just slightly hotter than the other scales, except for the comparison with Petigura et al. (2018a; K2 targets median difference = 8 K) and Martinez et al. (2019; median difference = 0 K).

Comparisons of the surface gravities derived here—from Fe I and Fe II ionization balance—with those from the works discussed above are shown in Figure 6 (as in Figure 5, the median differences ("Other Work"—"This Work") ± MAD are given in each panel). The median log g differences for all studies and the surveys are surprisingly small (see Section 4.1.1) given the different analysis methodologies and line lists, all <0.06 dex, except for Petigura et al. (2018a) that has a mean log g difference of 0.12 dex. In all comparisons the MAD values are smaller or equal to 0.14 dex, which is smaller than typical uncetainties in log g values.

4.1.1. Asteroseismic versus Spectroscopic Surface Gravities

The stellar parameters derived here (T_{eff}, log g, ξ, and [Fe/H]) are based on an analysis of a sample of Fe I and Fe II lines, where correlations between parameters in such a spectroscopic analysis can lead to systematic errors, especially in the derived values for log g; for example, Fe I lines are typically stronger than Fe II lines, leading to potential correlations between the microturbulent velocity and log g. Accurate surface gravities can thus be one of the more difficult parameters to constrain via spectroscopy, especially if the Fe II lines are few in number and weak. In order to investigate possible systematic offsets in the log g values derived in this study, we compare our results with those computed via asteroseismology, where the surface gravity can be derived with quite good precision (Pinsonneault et al. 2018).

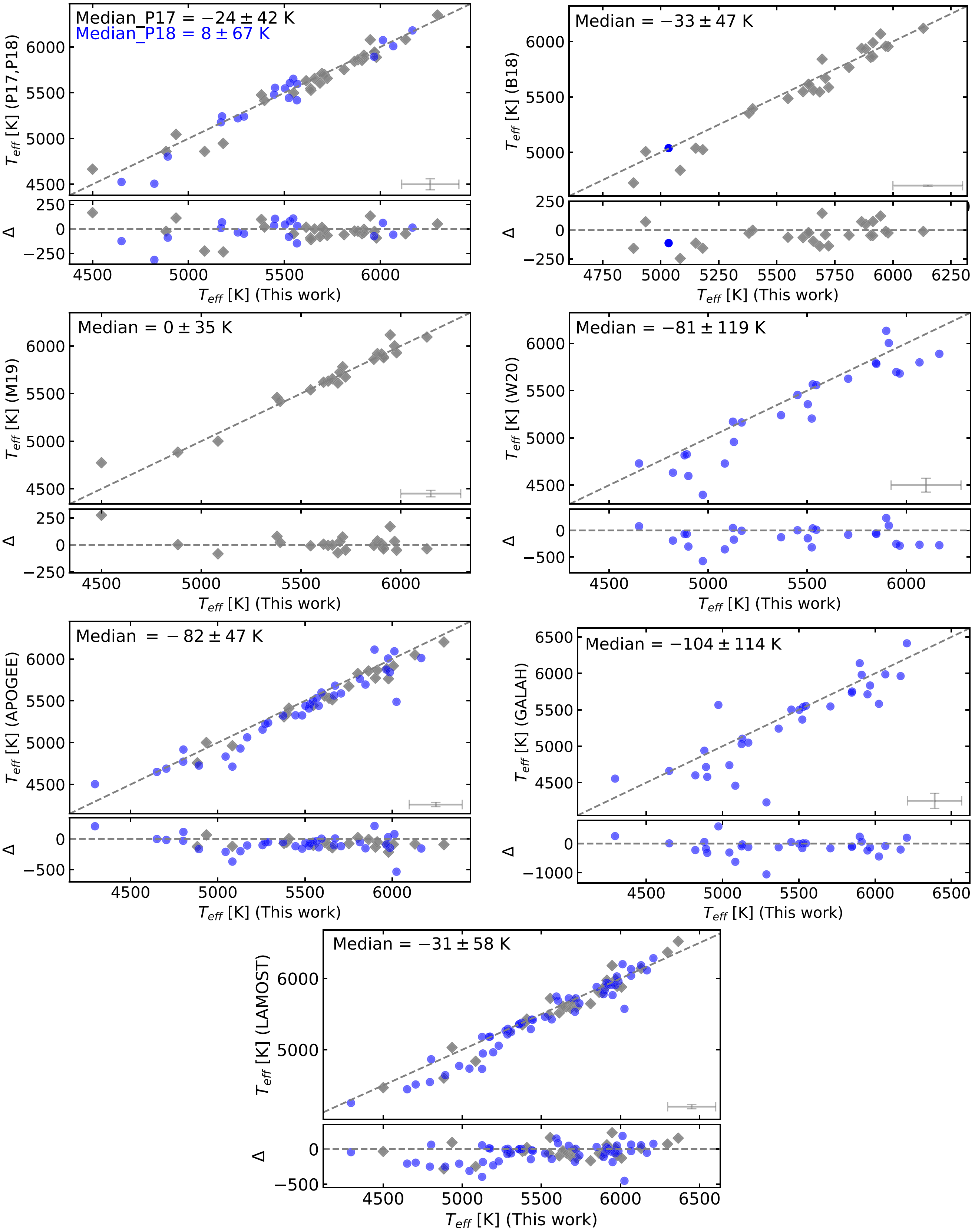

Figure 5. Comparisons of the effective temperatures in this study with those from Petigura et al. (2017, 2018a; P17 and P18, respectively), Brewer & Fischer (2018; B18), Martinez et al. (2019; M19), Wittenmyer et al. (2020; W20), APOGEE DR17, GALAH DR3, and LAMOST DR5. K2 stars are blue circles and Kepler 1 stars are gray diamonds. The bottom subpanels show the difference between "Other Work–This Work" (Δ). The median differences between the parameters and the corresponding MAD are indicated in each case. The black dashed lines represent equality.

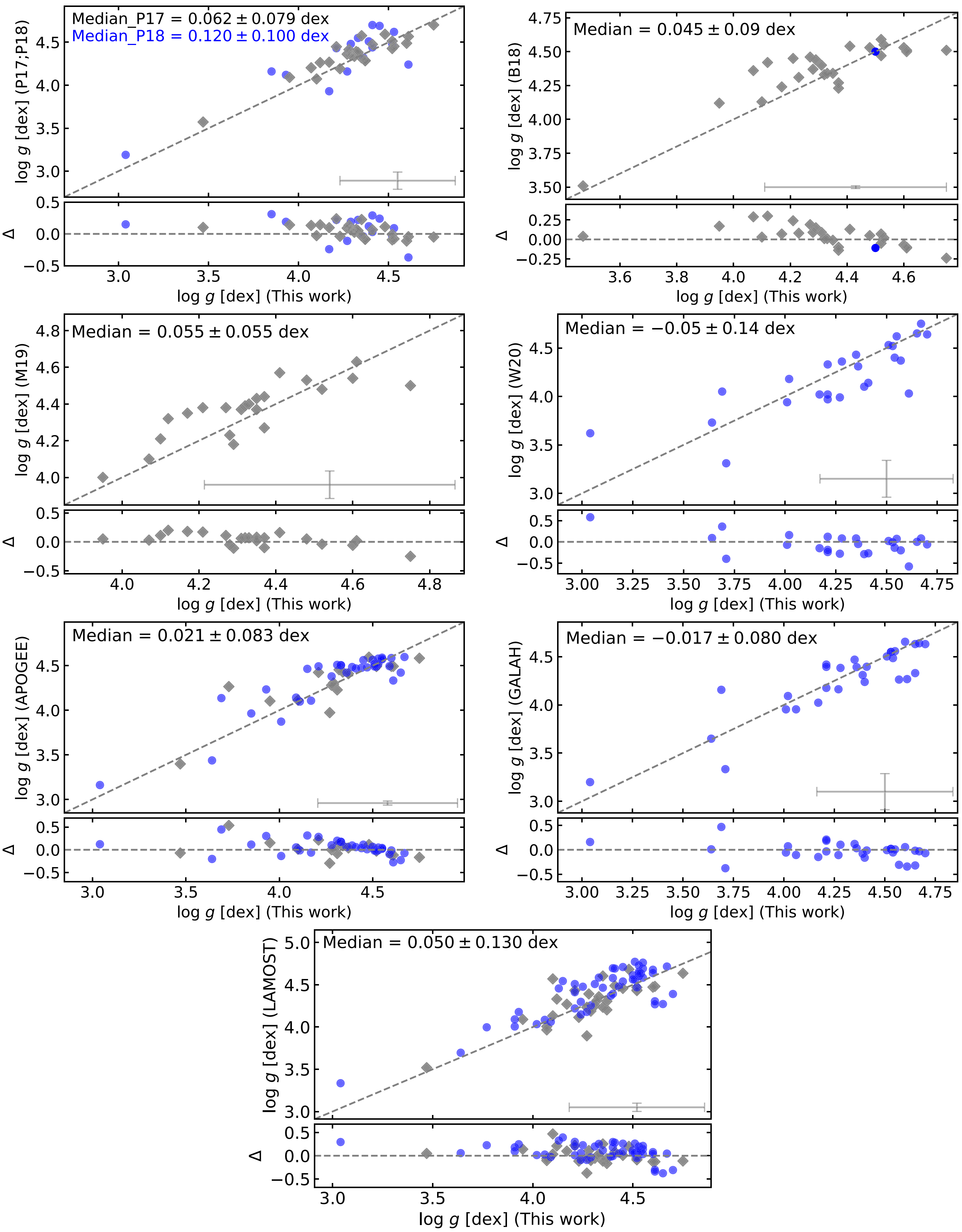

Figure 6. Comparison of the log g values derived in this work and Petigura et al. (2017, 2018a; P17 and P18, respectively), Brewer & Fischer (2018; B18), Martinez et al. (2019; M19), Wittenmyer et al. (2020; W20), APOGEE DR17, GALAH DR3, and LAMOST DR5 for K2 stars (blue circle) and Kepler 1 stars (gray diamond). The median differences between the parameters and the corresponding MAD are indicated in each case. The black dashed lines represent equality. Each bottom subpanel plots the difference, Δ, between "Other Work–This Work."

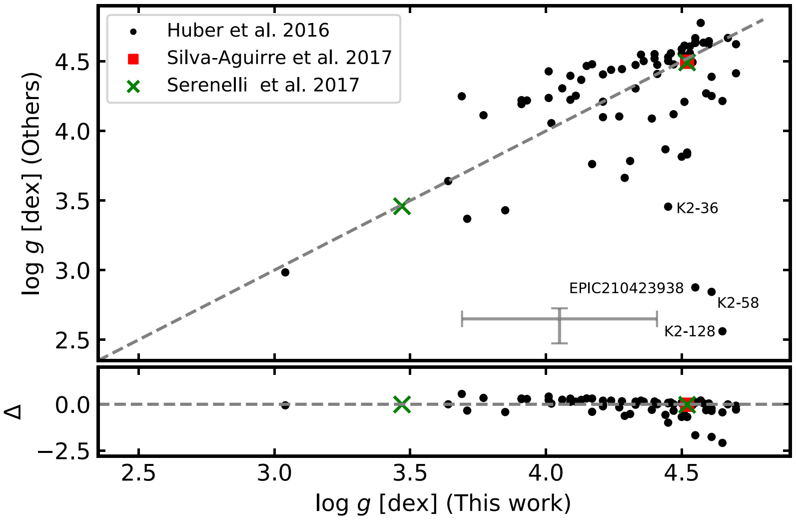

Figure 7. Comparisons of spectroscopic surface gravities derived in this work with asteroseismic surface gravities from Huber et al. (2016), Aguirre et al. (2017), and Serenelli et al. (2017). The four most discrepant values of stellar log *g* between this work and Huber et al. (2016) are labeled and these are discussed in the text. The bottom panel shows the differences between "Other Work–This Work." Median uncertainty error bars are presented.

For such a comparison, we collected in Figure 7 asteroseismology results for 83 stars from Huber et al. (2016), Aguirre et al. (2017), and Serenelli et al. (2017). In order to compute surface gravities via asteroseismology, Huber et al. (2016) and Serenelli et al. (2017) used the $T_{\rm eff}$ and [Fe/H] from the APOGEE survey (DR13), while Aguirre et al. (2017) adopted $T_{\rm eff}$ and [Fe/H] from several literature sources. Most of the stars in common with this study are from Huber et al. (2016); the log *g* values from that study show no significant offsets and are in good agreement when compared to ours, with a median log *g* difference ("Huber et al. 2016–This Work") = 0.033 ± 0.164 dex. However, there are four stars for which the log *g* differences are >1 dex. These four discrepent stars (which are labeled in Figure 7) have asteroseismic gravities that would indicate that they are giant or subgiant stars, whereas other studies have derived surface gravities that suggest that these stars are dwarfs as discussed below:

1. K2-36: this star was analyzed individually by Damasso et al. (2019) using high-resolution spectra from HARPS-N, with stellar parameters derived using the spectroscopic technique and finding log *g* values of 4.73, 4.60, and 4.57 with EWs, Atmospheric Stellar Parameters from Cross-Correlation Functions (CCFpams), and Stellar Parameter Classification (SPC; Buchhave et al. 2014), respectively. Using `SME` and `SpecMatch` with HIRES spectra, Sinukoff et al. (2016), Brewer et al. (2016), and Crossfield et al. (2016) derived log *g* = 4.65, 4.55, and 4.60, respectively. Finally, using SPC in Tillinghast Reflector Echelle Spectrograph (TRES) spectra, Vanderburg et al. (2016) derived log *g* = 4.70. Our result (log *g* = 4.45) is ∼0.1–0.3 dex lower than these studies, although all of these results indicate that K2-36 is a dwarf.
2. K2-58: using `SpecMatch` and `SME` with HIRES spectra, Crossfield et al. (2016) and Brewer & Fischer (2018) derived log *g* = 4.52 and 4.50, respectively. Using `SPC` with TRES spectra, Vanderburg et al. (2016) derived log *g* = 4.54, with these values being consistent with our log *g* = 4.50 dex, pointing to K2-58 as being a dwarf.
3. K2-128: using `SPC` with TRES spectra, Crossfield et al. (2018) and Mayo et al. (2018) derived log *g* = 4.70; while this result is 0.20 dex larger than our log *g*, taken together, these studies point to K2-128 as being a dwarf.
4. EPIC 210423938: for this star, the log *g* value obtained by Mayo et al. (2018) is 4.69. Stassun et al. (2019) determined that log *g* = 4.55 from its stellar radius and mass. Considering our result (log *g* = 4.55 dex), we identify EPIC 210423938 as a dwarf.

In summary, spectroscopic studies have found the four stars discussed above to have dwarf-star surface gravities. In addition, this status is confirmed from their DR3 Gaia parallaxes and distances, with distances to K2-36 of 109 pc, K2-58 of 182 pc, K2-128 of 114 pc, and EPIC 210423938 of 149 pc, resulting in absolute Gaia or V magnitudes of $M_V = 6.5$, $M_G = 5.8$, $M_V = 7.3$, and $M_V = 7.1$, respectively. These absolute magnitudes confirm them as K dwarfs. Without considering the four discrepant stars discussed above, we find median log *g* differences with Huber et al. (2016) = −0.049 ± 0.136. We note that for the few stars in common with Aguirre et al. (2017) and Serenelli et al. (2017), there is excellent agreement.

4.2. Metallicities

Figure 8 summarizes a comparison of the metallicities for K2 stars (blue circles) and Kepler 1 stars (gray diamonds) derived in this work with those derived in other studies and surveys. The metallicities from the literature were obtained either via spectrum synthesis methods (Petigura et al. 2017, 2018a; Brewer & Fischer 2018; Wittenmyer et al. 2020), (Buder et al. 2021; GALAH), (Jonsson et al. 2020; APOGEE), (Zong et al. 2018; LAMOST) or were based on EW measurements of Fe I and Fe II lines (Ghezzi et al. 2021). For Kepler 1 stars in common with Petigura et al. (2017), the median metallicity difference is 0.040 ± 0.034 dex, while with Brewer & Fischer (2018) it is 0.024 ± 0.064 dex. There are 22 stars in common with Ghezzi et al. (2021), with a median difference of 0.017 ± 0.037 dex. The K2 stars in common with Petigura et al. (2018a) have a median difference of 0.021 ± 0.052 dex, and for those in common with Wittenmyer et al. (2020) the

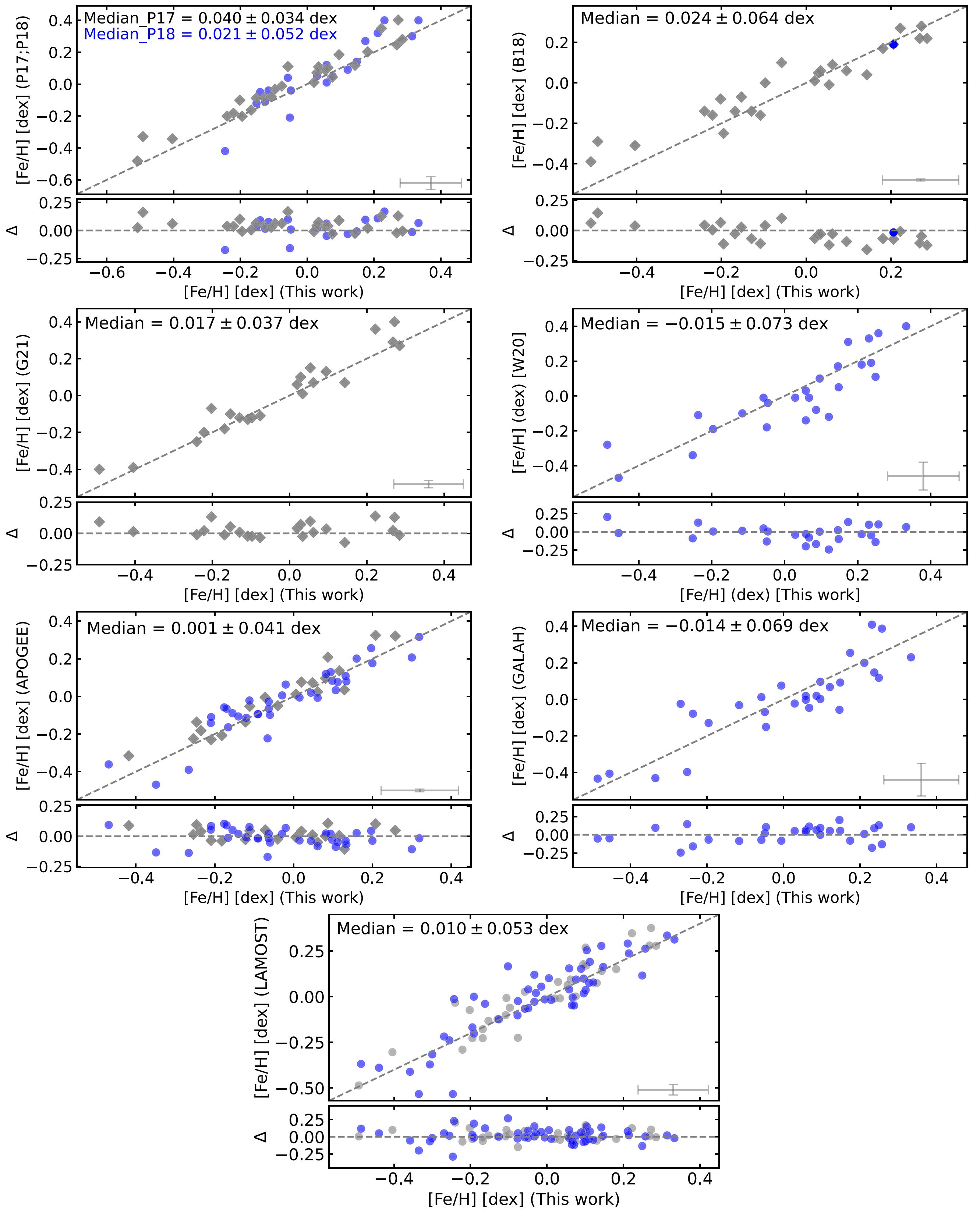

Figure 8. Comparisons of metallicities derived in this work with results from Petigura et al. (2017, 2018a; P17 and P18, respectively), Brewer & Fischer (2018; B18), Ghezzi et al. (2021; G21), Wittenmyer et al. (2020; W20), APOGEE DR17, GALAH DR3, and LAMOST DR5, for K2 stars (blue circles) and Kepler 1 stars (gray diamonds). The median differences between the parameters and the corresponding MAD scatters are indicated in each case. The black dashed lines represents equality. The bottom subpanels show the differences between "Other Work–This Work."

median [Fe/H] difference is -0.015 ± 0.073 dex. Comparison of the metallicities with the spectroscopic surveys also finds excellent agreement: 0.001 ± 0.041 dex for APOGEE DR17, while with GALAH DR3 it is -0.014 ± 0.069 dex. Finally, the median difference for stars in common with LAMOST DR5 is 0.010 ± 0.053 dex.

Overall, the metallicity comparisons in Figure 8 indicate good consistency between our results and the other metallicity scales, with median metallicity differences in all cases being smaller than ~0.04 dex and MAD less than 0.07 dex. Save for a few outliers, the scatter in the [Fe/H] differences are well within the expected uncertainties.

4.3. Stellar Radii and Masses

A number of studies in the literature obtained stellar radii and, in some instances, also masses, for Kepler 1 targets using different combinations of codes, models, and parameters. Johnson et al. (2017) used the isochrone method, stellar parameters from Petigura et al. (2017), and Dartmouth Stellar Evolution Program (DSEP) models (Dotter et al. 2008); Fulton & Petigura (2018), computed stellar radii using Gaia DR2 inverted parallaxes, and Martinez et al. (2019) used their stellar parameters, combined with the Gaia DR2 distances from Bailer-Jones et al. (2018). The large Gaia–Kepler stellar properties catalog by Berger et al. (2020b) combined isochrones, Gaia DR2 parallaxes, and spectroscopic metallicities using the `isoclassify` (Huber et al. 2017) package, while Hardegree-Ullman et al. (2020) used stellar parameters from LAMOST and derived K2 stellar radii from the Stefan–Boltzmann law and stellar masses from stellar radii. Via asteroseismology, Huber et al. (2016) also derived the stellar masses and radii of K2 stars using $T_{\rm eff}$ and [Fe/H] from APOGEE DR14, while Mayo et al. (2018) used the `isochrone` package (Morton 2015), which requires the effective temperature, surface gravity, and metallicity as input parameters (these parameters were derived using the spectral synthesis method described by Mayo et al. 2018).

Comparisons of our derived radii (Section 3.3) with those in the six studies mentioned above are shown in the left and right panels of Figure 9, respectively for K2 and Kepler 1 targets. Please note the different scales for the x- and y- axes in the different panels. First, when considering the median radius differences "Other works–This work," overall, there is not a clear bias in any direction. Overall, all results from the literature present similar levels of consistency relative to ours. We note, however, the presence of the four significant outliers of Huber et al. (2016) for which their radii are much larger than ours (the log g values for these cases are also very discrepant as discussed in Section 4.1.1 and shown in Figure 7), which when removed improve the consistency relative to our results ($0.029 \pm 0.082\ R_\odot$).

For example, for the most discrepant case (K2-128), the stellar radius of Huber et al. (2016) would be roughly 15 times larger than ours, which would imply a correspondingly larger planet radius. For the comparisons with Berger et al. (2020b), Mayo et al. (2018), and Martinez et al. (2019), the median differences are $\Delta R_{\rm star} < -0.01\ R_\odot$, noting again the presence of outliers. In the comparison with Mayo et al. (2018), in particular, the outliers are mostly for radii larger than ~1.5 $R_\odot$, with a tendency that our radii are larger. For the comparisons with Hardegree-Ullman et al. (2020) and Johnson et al. (2017), the systematics go in the opposite direction, with median $\Delta R_{\rm star} \sim\ 0.03\ R_\odot$. In all comparisons, the MADs are less than 0.05 $R_\odot$, except for Johnson et al. (2017) that is slightly larger (0.07 $R_\odot$), while Huber et al. (2016) has a much larger MAD of 0.08 $R_\odot$.

Moving on to discuss the stellar masses derived in this study, comparisons with other results are shown in Figure 10. The mass scale from Mayo et al. (2018) has a median difference (and MAD) that are very small when compared to ours, indicating overall good agreement. We note, however, that for stars more massive than $M_{\rm star} \sim 1.1\ M_\odot$, there is significantly more scatter, while for stars with $M < 1.1\ M_\odot$ we find a median mass difference of $0.026 \pm 0.020\ M_\odot$. The mass comparisons for the Kepler 1 stars (Johnson et al. 2017; Berger et al. 2020a; right panels of Figure 10), indicate even smaller offsets, where, the median mass differences are less than 3% and the MADs are $\Delta M_{\rm star} \sim 0.03\ M_\odot$, although there are also outliers in these comparisons. The median difference for stars with less than 1 $M_\odot$ are $-0.009 \pm 0.025\ M_\odot$ and $0.003 \pm 0.021\ M_\odot$ for Johnson et al. (2017) and Berger et al. (2020a), respectively. The mass scale of Hardegree-Ullman et al. (2020), on the other hand, has a larger systematic offset when compared to ours, being overall more massive than our scale by ~8.2%; the latter comparison also shows some scatter with an rms value of 0.22 and a MAD of 0.111 $M_\odot$, which is the largest in Figure 10.

Asteroseismic masses are, in principle, the most accurate masses presented in Figure 10, having the smallest expected uncertainties (Pinsonneault et al. 2018). When compared to our results, there is a clear systematic difference between the mean mass of Huber et al. (2016) and ours, with our masses being smaller than the asteroseismic ones in the median by ~3%. We note for example, the significant outlier that appears as much more massive ($M_{\rm star} =\ 1.2\ M_\odot$) when compared to our mass value ($M_{\rm star} \sim 0.7\ M_\odot$) and again refer to the discussion in Section 4.1.1. As in the comparison with Mayo et al. (2018), there is also more scatter for stars with masses larger than 1.1 $M_\odot$.

4.4. Planetary Radii

The radii of exoplanets orbiting Kepler 1 and K2 host stars have been derived in several studies in the literature and these are compared with our results in the different panels of Figure 11. Here, the planetary radii were computed using Equation (1), which combines our derived stellar radii with transit depth values available in the literature (Section 3.3), and these are presented in Table 6, which contains the star identifications, the planet names, transit depths, and planetary radii along with the error in $R_{\rm pl}$.

For K2, we compare planetary radii with those of Petigura et al. (2018a), Hardegree-Ullman et al. (2020), Kruse et al. (2019), Mayo et al. (2018), Vanderburg et al. (2016), and Crossfield et al. (2016). Overall, the results in Figure 11 indicate that our planetary radii for K2 hosts are, on the median, larger than in the other K2 works, except for Crossfield et al. (2016); however, the median differences in the planetary radii ("Other Work–This Work") are small, with median systematic differences (("Other Work–This Work")/"This Work") of 0.2% for Crossfield et al. (2016), ~2% for Kruse et al. (2019), ~3% for Hardegree-Ullman et al. (2020) and Vanderburg et al. (2016), and ~4% for Mayo et al. (2018). Although the median differences are, in some cases insignificant (at the level of 0%–2%), or small (at the level of 3%–4%), there are some outliers with larger

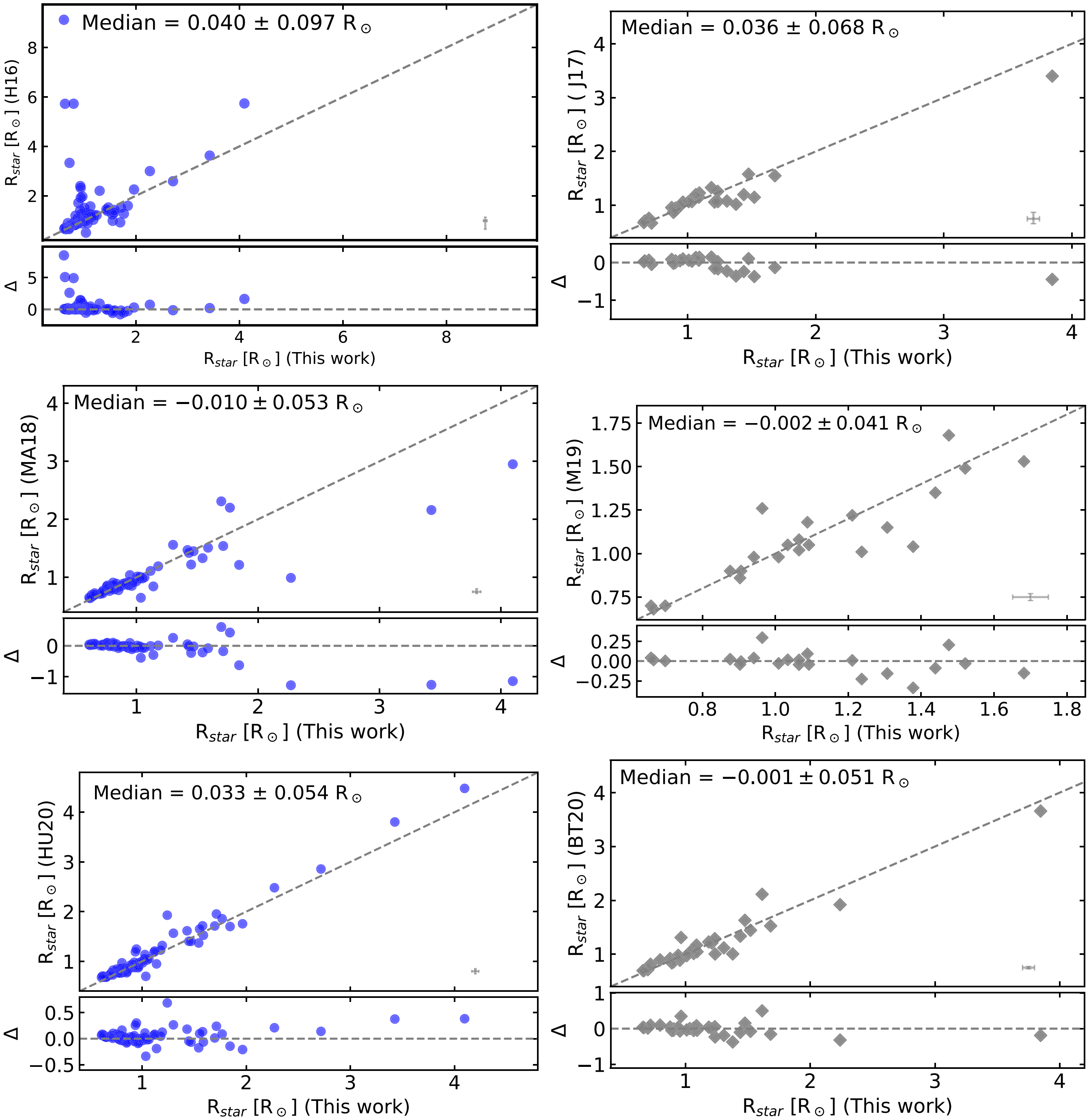

Figure 9. Comparisons of the stellar radii derived in this work with stellar radii from Huber et al. (2016; H16), Mayo et al. (2018; MA18) and Hardegree-Ullman et al. (2020; HU20) for K2 stars (left panels), and Johnson et al. (2017; J17), Martinez et al. (2019; M19) and Berger et al. (2020a; BT20) for Kepler 1 stars (right panels). The four most discrepant radii between this study and Huber et al. (2016) are discussed in the text. Each bottom subpanel shows the difference, Δ = "Other Work–This Work."

discrepancies in some regimes, as is the case of the comparison with Vanderburg et al. (2016) that reveals larger offsets, in particular for planets with radii larger than ∼2.5 $R_\oplus$. The comparison with Petigura et al. (2018a) finds larger median differences with our derived planetary radii of ∼6% larger.

In this comparison (top left panel), there is one significant outlier in the small planet regime, planet K2-183d, for which we find $R_{\rm pl} = 3.1\ R_\oplus$, while Petigura et al. (2018a) find $R_{\rm pl} = 17.4\ R_\oplus$. Our result is better agreement with the planet radius reported by Livingston et al. (2018) ($R_{\rm pl} = 2.9 R_\oplus$) and Mayo et al. (2018) ($R_{\rm pl} = 2.5\ R_\oplus$), as well as by Hardegree-Ullman et al. (2020) ($R_{\rm pl} = 5.1\ R_\oplus$) and Kruse et al. 2019) ($R_{\rm pl} = 5.2\ R_\oplus$). We also note that the difference in the effective temperature between Petigura et al. (2018a) and our result is $\Delta T_{\rm eff} = -81$ K and that if we used Petigura et al. (2018a) $R_{\rm pl}/R_{\rm star}$ value we would obtain $R_{\rm pl} = 17.56\ R_\oplus$, which is in much closer agreement with Petigura et al. (2018a), indicating that the difference in transit depth is responsible for a large part of the difference in $R_{\rm pl}$.

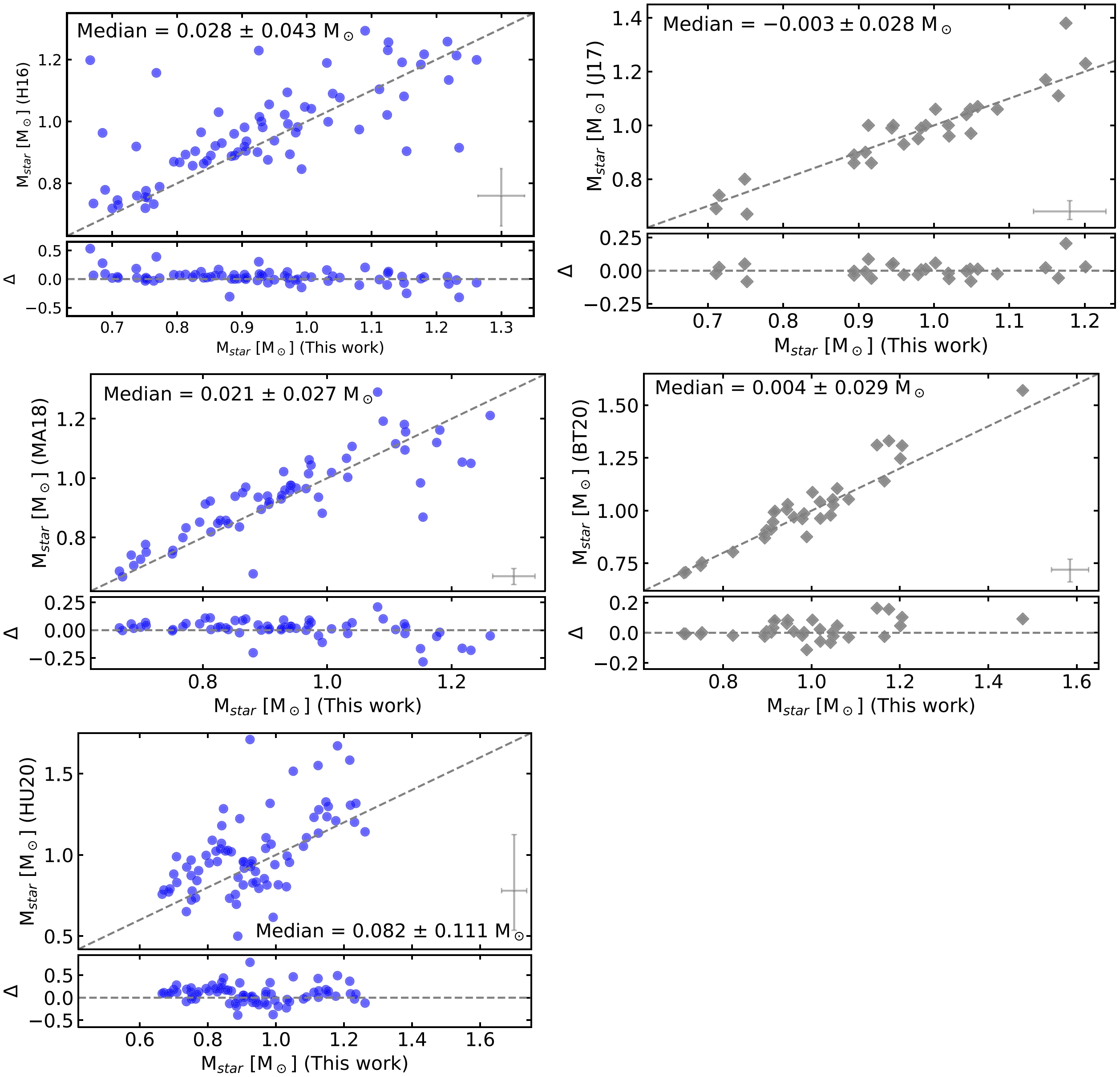

Figure 10. Comparisons between the derived stellar masses in this study with those from Huber et al. (2016; H16), Mayo et al. (2018; MA18) and Hardegree-Ullman et al. (2020; HU20) for K2 stars (left panels), and Johnson et al. (2017; J17) and Berger et al. (2020a; BT20) for Kepler 1 stars (right panels). The bottom subpanels show the differences, Δ, between "Other Work–This Work."

For the Kepler 1 planets studied here, the radii of Petigura et al. (2022) and Fulton & Petigura (2018) show the largest offsets relative to our results, with a median systematic difference of 8%–9%, again with our planetary radius scale being larger. For Martinez et al. (2019), there is a much smaller systematic shift in the planetary radii relative to ours of ∼1%, and also having the smallest MAD of all comparisons, indicating that the scales for planetary radii are very consistent in both studies.

One aspect to keep in mind is the fact that the various studies discussed here may have employed different transit depths. Some studies, such as ours, use literature values, while others derive their own. For planets in common, we should note that we used the transit depths from Kruse et al. (2019) and these were also used by Hardegree-Ullman et al. (2020), while Vanderburg et al. (2016), Crossfield et al. (2016), Mayo et al. (2018), and Petigura et al. (2018a) derived their own transit depths. For the Kepler 1 planets, we used the transit depths from Thompson et al. (2018), which are also used by Martinez et al. (2019) and Petigura et al. (2022), while the transit depths of Fulton & Petigura (2018) come from Mullally et al. (2015).

5. Discussion

The stellar parameters obtained for the 115 stars analyzed in this study, along with those for the solar proxies Astraea and Parthenope, are summarized in Figure 12 as a Kiel diagram, with log g plotted as a function of $T_{\rm eff}$ and the stars shown as filled circles color-coded by their iron abundance; the color bar represents the metallicities. Results for the solar proxies are shown as black stars. The dashed lines are the Yonsei–Yale isochrones (Yi et al. 2001, 2003;

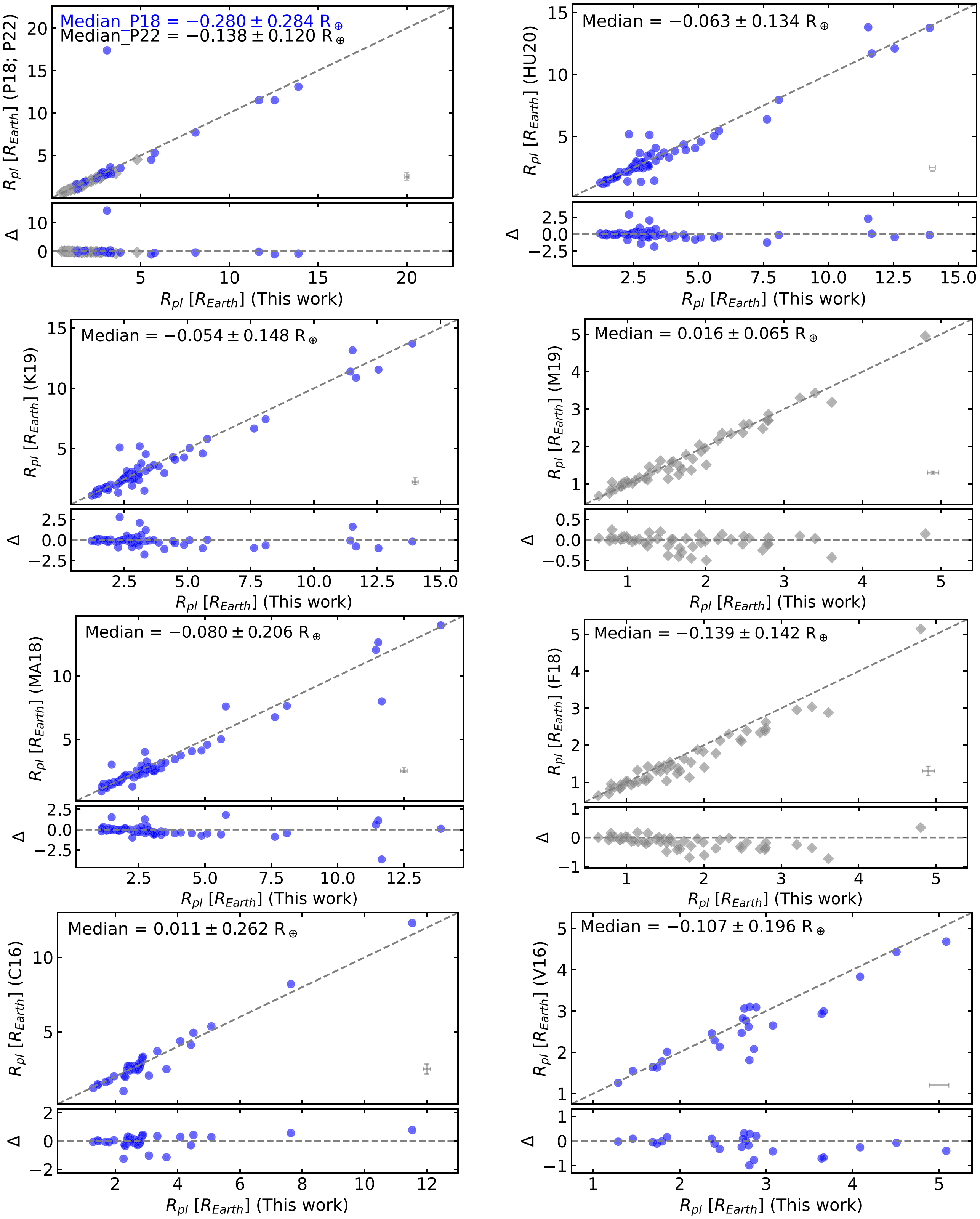

Figure 11. Comparison of the derived planetary radii with the literature values. Blue circles represent the planets of K2 host stars and gray diamonds of Kepler 1 host stars; beginning in the top left panel and preceeding clockwise, the comparisons are with Petigura et al. (2018a, 2022; P18 and P22, respectively), Hardegree-Ullman et al. (2020; HU20), Kruse et al. (2019; K19), Martinez et al. (2019; M19), Mayo et al. (2018; MA18), Fulton & Petigura (2018; F18), Crossfield et al. (2016; C16), and Vanderburg et al. (2016; V16). The bottom subpanels present the differences, Δ, of "Other Work–This Work."

Demarque et al. 2004; Han et al. 2009) corresponding to an age of 4.6 Gyr and metallicities between −0.6 and 0.2 dex, with steps of 0.2 dex. As can be seen from the locations of the points in this diagram, most of the stars in our sample are on, or near, the main sequence, but there are also a small number of stars that are clearly evolved.

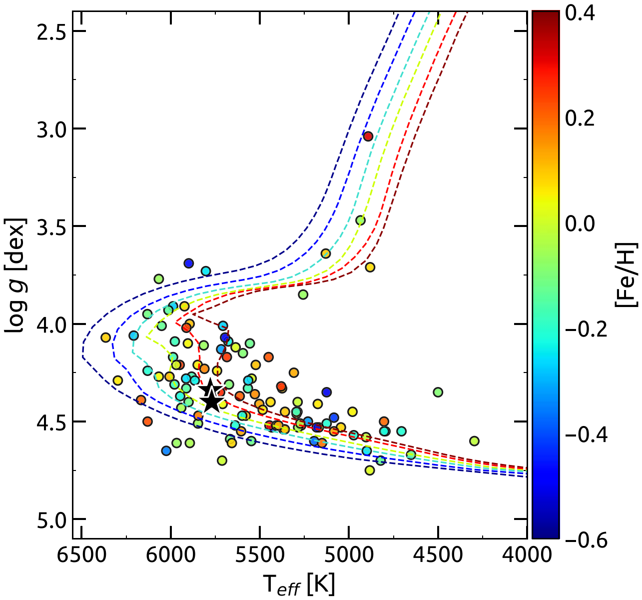

Figure 12. Kiel diagram for the sample stars. Dashed lines represent 4.6 Gyr old stellar evolution tracks from Yonsei–Yale isochrones for different metallicities: −0.6, −0.4, −0.2, 0.0, 0.2, and 0.4 dex. The colors of circles represent different metallicities as shown by the color bar.

Table 6
Planetary Radii

Star ID	Planet Name	ΔF (ppm)	$R_{\rm pl}$ ($R_\oplus$)	δ $R_{\rm pl}$ ($R_\oplus$)
EPIC201577035	K2-10 b	1691.0	4.09	0.14
EPIC211990866	K2-100 b	122.5	1.36	0.04
EPIC211913977	K2-101 b	749.0	2.17	0.08
EPIC211970147	K2-102 b	200.0	1.09	0.09
EPIC211525389	K2-105 b	1338.0	3.86	0.14
EPIC220674823	EPIC220674823 b	284.7	1.78	0.06
EPIC220674823	EPIC220674823 c	903.0	3.17	0.10
EPIC211736671	K2-108 b	973.0	5.78	0.45
EPIC201596316	K2-11 b	916.0	2.72	0.11
…	…	…	…	

Note. Transit depths (ΔF) are collected from Kruse et al. (2019) and where available for K2 planets, while for Kepler 1 planets they are from Thompson et al. (2018). This table is published in its entirety in the machine-readable format. A portion is shown here for guidance regarding its form and content.

(This table is available in its entirety in machine-readable form.)

Focusing initially on our results for the K2 sample, Figure 13 uses histograms to illustrate the distributions of effective temperature and surface gravity in the top left and right panels, respectively. Our target selection was biased, as it avoided M dwarfs, and most of the K2 stars in this sample have effective temperatures between ∼4800—6000 K, with a peak at roughly $T_{\rm eff} \sim 5500$ K (median = 5503 K; MAD = 346 K). The log g distribution of the K2 stars in this study is dominated by stars having values between log $g \sim 4.2$ and 4.6, with a median log $g = 4.41$ (MAD = 0.14; 16th percentile = −0.36; 84th percentile = 0.14).

The bottom panels of Figure 13 show the distributions of the derived stellar masses (left bottom panel) and radii (right bottom panel) for the K2 targets. The median of the mass distribution of the K2 sample studied here is just below the solar value of $M_{\rm star} = 0.93 \pm 0.11\ M_\odot$, with all K2 stars having masses between $M_{\rm star} = 0.6$–$1.3\ M_\odot$. This is a narrower mass range than that found for the 2956 Kepler hosts by Berger et al. (2020a), which covers $M_{\rm star} = 0.5$–$1.7\ M_\odot$, noting however that their median stellar mass ($M_{\rm star} = 0.99 \pm 0.2\ M_\odot$) is just slightly larger than our K2 sample. The K2 C5 sample of Zink et al. (2020) has a similar median mass of $M_{\rm star} = 0.92^{+0.34}_{-0.18}$ $M_\odot$, but which extends over a much larger range in mass, from ∼0.1 to 2.5 $M_\odot$.

The stellar radii distribution of the studied K2 sample (shown in the right bottom panel of Figure 13), has a median radius of $R_{\rm star} = 0.94\ R_\odot$ (16th percentile = −0.22; 84th percentile = 0.59), with very few stars in our sample having radii larger than $R_{\rm star} > 2\ R_\odot$. An investigation of the mass–radius relation indicates that the four stars in our K2 sample having radii $R_{\rm star} > 2\ R_\odot$ and log g values smaller than 3.8 all have masses larger than 1.1 $M_\odot$, indicating that they have evolved away from the main sequence over realisitic timescales (∼7 − 8 Gyr for 1.1 $M_\odot$).

In Figure 14 we show the metallicity distributions on the left panel, along with the cumulative distribution functions on the right panel for the K2 sample (shown in blue) and the CKS sample analyzed by Ghezzi et al. (2021) (shown in red). The metallicity distribution of our K2 sample covers the range between [Fe/H] = −0.5 to 0.3 (iron abundances roughly between $7.00 < A({\rm Fe}) < 7.80$), with ∼12% of stars being more metal-poor than [Fe/H] = −0.2. The median (±MAD) metallicity of the distribution is [Fe/H] = −0.03 ± 0.14 dex (A(Fe) = 7.49 ± 0.14 dex) and this value is very close to the metallicity obtained here for the solar-proxy asteroids (A(Fe) >= 7.52), and also in good agreement with the solar Fe abundance of Magg et al. (2022) (see Section 3.2). Overall the range in metallicity of our K2 sample overlaps roughly with that of the Galactic thin disk, although the K2 sample is slightly more metal-poor. The comparison with the metallicity distribution of the CKS sample of Ghezzi et al. (2021) also indicates that our K2 sample is more metal-poor, which is in line with the finding of Ghezzi et al. (2021) that the CKS metallicity distribution was akin to the metallicity distribution function (MDF) of the solar neighborhood based on stellar samples with Galactocentric distances between 7 kpc < Rg < 9 kpc from the APOGEE and GALAH surveys (Hayden et al. 2015, 2020); the metallicity distribution of APOGEE red giants is also shown as the black curve in Figure 14 for comparison. We can see that the distribution of both the K2 sample and the Ghezzi et al. (2021) CKS sample have a peak at [Fe/H] = 0.1 dex that is not well matched by the metallicity distribution of red giants in APOGEE. Compared to APOGEE, the K2 sample is relatively more metal-poor, not extending to [Fe/H] = 0.4, having fewer stars in the metal-rich end, and a more significant number of stars in the [Fe/H] = −0.2 bin than the APOGEE distribution. The median metallicity of the CKS sample is [Fe/H] = 0.06 ± 0.14 (Ghezzi et al. 2021), or, [Fe/H] = 0.04 ± 0.11 (Petigura et al. 2017); the K2 sample studied here is more metal-poor by −0.09 dex in the median, but we note that it is not as metal-poor as the K2 Campaign 5 sample analyzed by Zink et al. (2020), which has an approximately Gaussian distribution with a median [Fe/H] = −0.14 ± 0.18.

5.1. *Planetary Radii and the Radius Gap*

The final distribution of planetary radii derived from the Hydra spectra of K2 host stars contains 85 confirmed planets

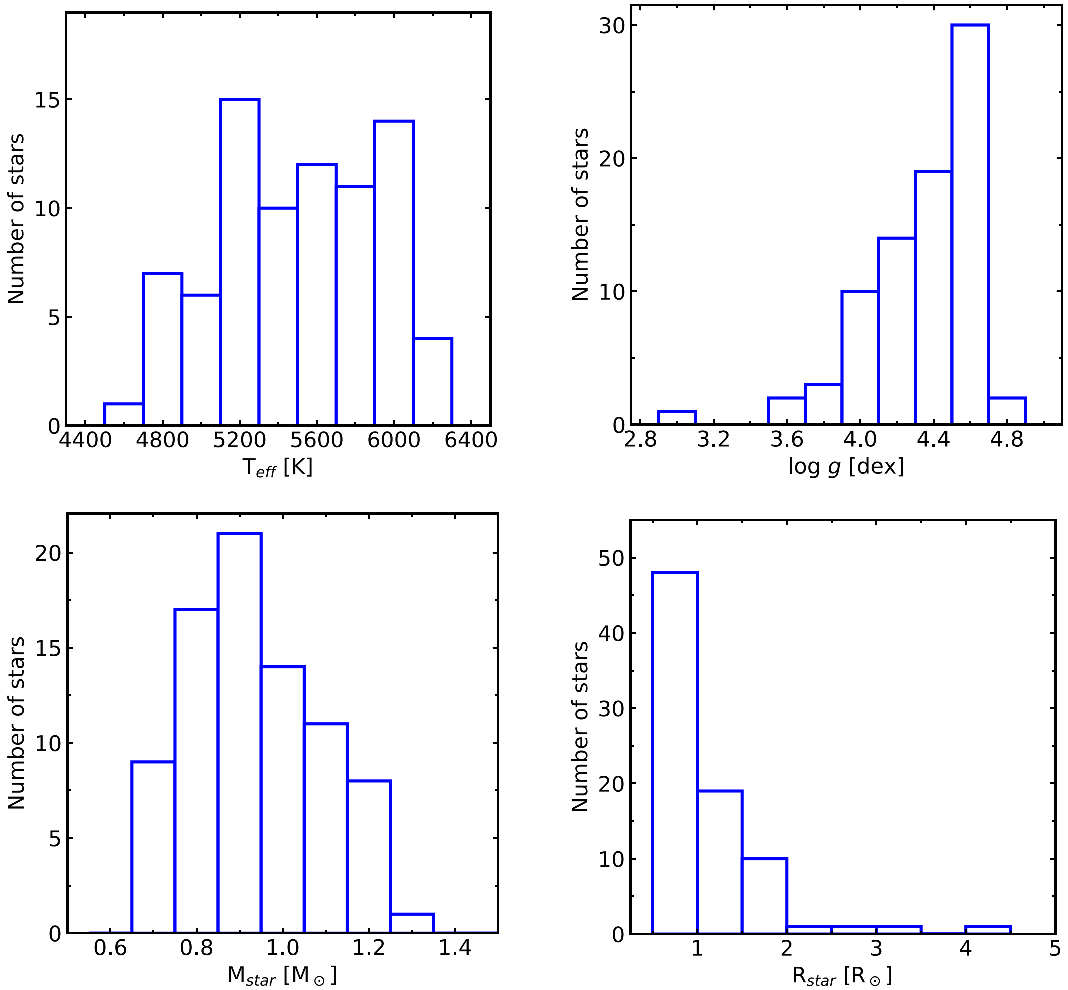

Figure 13. Effective temperature, surface gravity, mass, and radius distributions for the K2 stellar sample.

orbiting 69 stars. Although this sample is relatively small, the results presented here are derived using an independent methodology that relies on an analysis of a carefully selected set of Fe I and Fe II lines, which are used to determine fundamental host-star parameters ($T_{\rm eff}$, log g, and [Fe/H]), and thus represent a useful addition to the growing number of independently derived K2 planetary radii. Figure 15 (top panel) presents a histogram of K2 planetary radii that result from the derived stellar radii combined with available transit depth catalogs. The 85 planets plotted in Figure 15 reveal a distinct and well-defined radius valley that spans $R_{\rm pl} \sim 1.6-2.2\ R_\oplus$, with a minimun near 1.9 $R_\oplus$. Figure 15 includes all planetary orbital periods which, for this sample, range from P ~ 0.5 days up to 53 days and it should be noted that, due to the differing observing techniques between Kepler 1 and K2, the sample studied here is biased toward shorter orbital periods when compared to Kepler 1 periods, e.g., the CKS sample. Nevertheless, the K2 radius valley observed in this sample, with a minimum at $R_{\rm pl} \sim 1.9\ R_\oplus$, is very similar to the results derived from the CKS sample from several studies (e.g., Fulton et al. 2017; Berger et al. 2018; Fulton & Petigura 2018; Van Eylen et al. 2018; Martinez et al. 2019).

The bottom panel of Figure 15 provides a comparison of radii derived for the CKS sample (all Kepler 1 planets) from Martinez et al. (2019; their Figure 11(d)). Comparing the top and bottom panels of Figure 15 illustrates the similarity in the location of the radius valley between the K2 and Kepler 1 samples. Although the Kepler 1 field focused on a single pointing, encompassing a limited Galactic longitude and latitude (l ~70°–8°, b ~10°–20°), the K2 fields were constrained by the ecliptic plane and thus ranged over a broader range of Galactic longitudes and latitudes. The similarity in the position of the radius valley suggests it to be a ubiquitous phenomenon among short-period planets across a broad range of Galactocentric distances in the thin and thick disk populations; Zink et al. (2021) arrived at this conclusion after their analysis of planetary radii in the K2 Campaign fields 1−8 and 10−18.

With the similarity in the position of the radius valley between the K2 and Kepler 1 samples (Mayo et al. 2018; Hardegree-Ullman et al. 2020; Zink et al. 2021), we next investigate planet radius as a function of orbital period, with Figure 16 plotting our planet sample in a period–radius plane. The top panel includes all planets (our full sample) in the different orbital periods, with the K2 planets plotted as black filled circles and the Kepler 1 planets plotted as open diamonds; blue symbols represent the median and MADs of the planetary radii and orbital period distributions for each planet size domain: super-Earths ($R_{\rm pl} \leqslant 2\ R_{\oplus;}$ square), sub-Neptunes ($2\ R_\oplus < R_{\rm pl} \leqslant 4.4\ R_\oplus$; circle), sub-Saturns ($4.4\ R_\oplus < R_{\rm pl} \leqslant 8\ R_\oplus$; triangle), and Jupiters ($8\ R_\oplus < R_{\rm pl} \leqslant 20\ R_\oplus$; star). These median values are overall similar to those for the

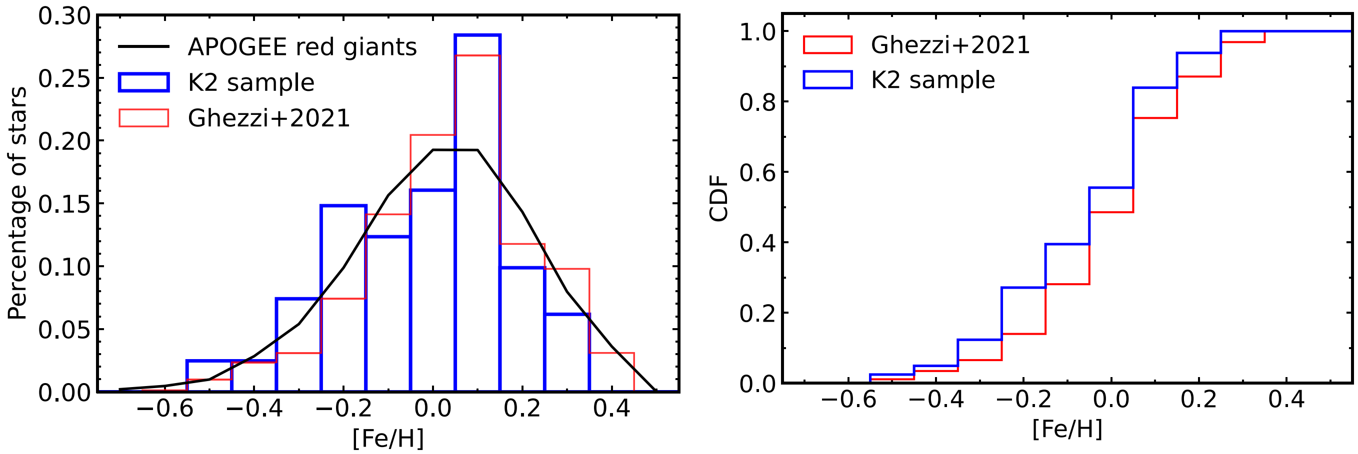

Figure 14. Iron abundance distributions (left panel) and cumulative distribution functions (right panel) for different samples of stars. The left panel presents the K2 sample studied here, shown as the blue histogram, and the CKS sample of Ghezzi et al. (2021) is shown in red, while the [Fe/H] distribution for the red giant stars in the local Milky Way disk from the APOGEE survey is shown as the black curve. The cumulative distribution functions for the K2 sample here and the CKS sample of Ghezzi et al. (2021) are compared in the right panel. Both panels show that the K2 sample studied here is slightly more metal-poor than both the CKS sample and the local disk.

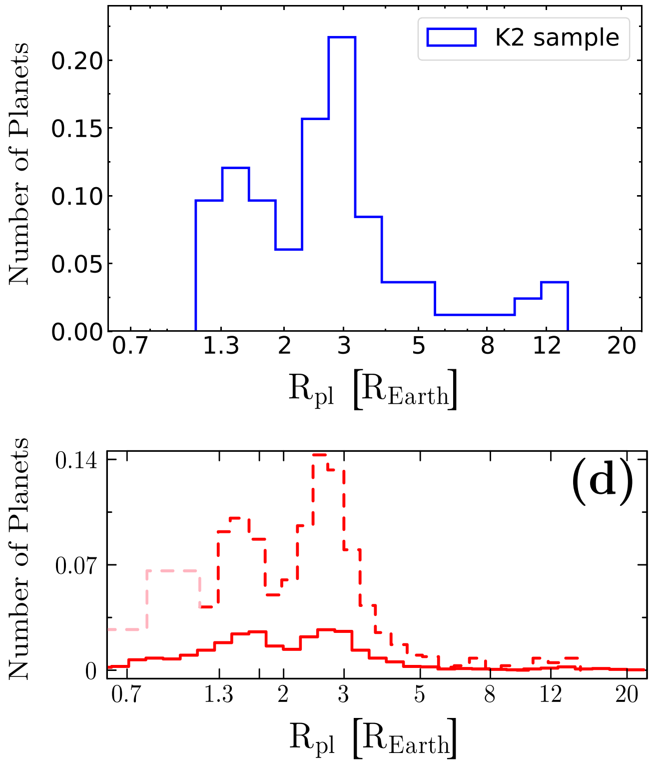

Figure 15. The top panel shows the planetary radius distribution for the K2 planet sample studied here, while the bottom panel shows the distribution of the CKS planet sample studied by Martinez et al. (2019), as shown in their Figure 11 panel (d). The red filled line histogram represents their sample and the red dashed line distribution takes into account completeness corrections. The location of the gap in the K2 (top panel) and CKS (bottom panel) radius distributions is approximately the same: $R_{\rm gap} \sim 2\ R_{\oplus}$.

CKS sample of Martinez et al. (2019), but here we adopt the limit of 4.4 $R_{\oplus}$ for the transition between sub-Neptunes and sub-Saturns, as discussed by Ghezzi et al. (2021).

Planetary radii $<4\ R_{\oplus}$ are shown in the bottom panels, where the bottom left panel plots only the sample of K2 planets, while in the bottom right panel includes all K2 planets and those Kepler 1 planets having orbital periods less than 100 days. In both plots the slope of the radius valley is shown as a blue line (we used the slope of −0.11 from Martinez et al. 2019). Although we do not fit a trend of the position of the radius gap, $R_{\rm gap}$, as a function of orbital period (P) to the 139 planets in our sample, the planetary radii that result from the stellar parameters derived here are consistent with the relation of the radius valley following a power law of the form $R_{\rm gap} \propto P^{-0.11}$, as shown in the bottom panels of Figure 16.

5.2. Planetary Radius, Orbital Period, and Stellar Metallicity

The distribution of host-star metallicity as a function of planetary radius is shown in the left panel of Figure 17. The 85 K2 planets in this study are the solid black circles and the Kepler 1 planets are the gray open diamonds. The blue symbols represent the median (±MAD) metallicities of the K2 planet hosts dividing the sample in the same planet size domains as in Figure 16: super-Earths, sub-Neptunes, sub-Saturns, and Jupiters. Although the K2 planet sample size is small, we find that, in general, the metallicities of the K2 planet hosts increase with planetary radius, but the increase in metallicity is seen in particular for the transition between the small (super-Earth and sub-Neptune) and large (sub-Neptune and sub-Saturn) planet regimes, a result that is similar to what has been found in previous studies of Kepler planets in the literature (Petigura et al. 2018b; Narang et al. 2018; Ghezzi et al. 2021; see also Beauge & Nesvorny 2013).

As mentioned in the introduction, previous works have investigated correlations between host-star metallicity and planet orbital period distributions, concluding that small and hot planets with orbital periods $P \lesssim 8$–10 days appear preferentially around metal-rich stars (e.g., Mulders et al. 2016; Wilson et al. 2018). The right panel of Figure 17 shows the host-star metallicity as a function of the planet orbital period for our studied sample (symbols are the same as in the left panel). The horizontal dashed lines represent the mean metallicities for those K2 planets having orbital periods below and above 10 days, and the 10 day boundary is marked as a dashed vertical line. We find that the median host-star metallicity for planets with $P < 10$ days is slightly metal-rich, 0.059 ± 0.122 dex, while the median host-star metallicity for planets with $P > 10$ days is slightly metal-poor, -0.060 ± 0.106 dex. Our K2 sample has mostly small planets and only some large planets. If we restrict the sample to that having only planets with $R_{\rm pl} < 4.4\ R_{\oplus}$, we obtain a similar behavior, with a median

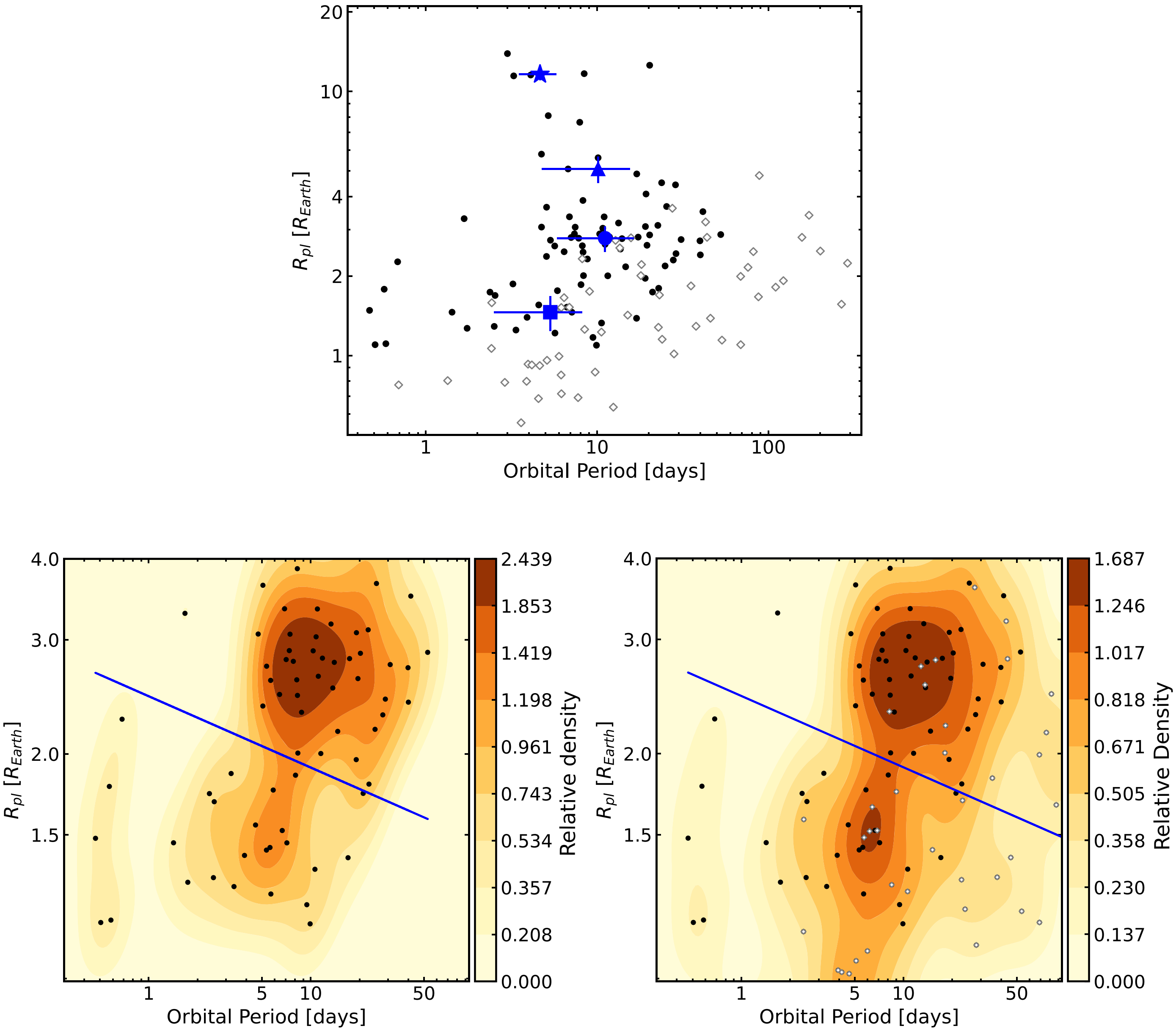

Figure 16. Planetary radius as a function of planetary orbital period. The top panel shows our sample of K2 planets (filled black circles) and Kepler 1 planets (open diamonds). The blue symbols are the median values of $R_{\rm pl}$ vs. orbital period for the Jupiters ($8\ R_{\oplus} < R_{\rm pl} \leqslant 20\ R_{\oplus}$), sub-Saturns ($4.4\ R_{\oplus} < R_{\rm pl} \leqslant 8\ R_{\oplus}$), sub-Neptunes ($2\ R_{\oplus} < R_{\rm pl} \leqslant 4.4\ R_{\oplus}$), and super-Earths ($R_{\rm pl} \leqslant 2\ R_{\oplus}$). The bottom left panel shows the K2 planets in our sample with $<4\ R_{\oplus}$ and in the bottom right panel we show the same but with the addition of the Kepler 1 planets in our sample. The slope of the radius valley vs. orbital period derived by Martinez et al. (2019) for the CKS sample is also shown for comparison purposes only. The color bar shows the relative density of detected planets in the P–$R_{\rm pl}$ plane using a Gaussian kernel density estimation (KDE).

metallicity of 0.051 ± 0.124 for $P < 10$ days and -0.051 ± 0.090 for planets with $P > 10$ days. We note that adopting a boundary at $R_{\rm pl} = 8.3\ R_{\oplus}$, as found by Wilson et al. (2018), gives similar metallicity differences between the two orbital period regimes. Summarizing the results obtained here for the K2 host-star metallicities and orbital planetary periods are in line with what was found previously for Kepler 1 systems.

6. Summary and Conclusions

We present effective temperatures, surface gravities, metallicities, and microturbulent velocities for 81 planet-hosting K2 stars based on a homogeneous spectroscopic analysis using a uniform set of high-resolution spectra from the WIYN/Hydra spectrograph covering a spectral window between 6050 and 6350 Å. Additionally, stellar parameters are presented for 33 planet-hosting Kepler 1 stars.

The calculations were done in LTE and we used Kurucz model atmospheres. The stellar parameters and metallicities were derived from measurements of the EWs of Fe I and Fe II lines and from requiring excitation and ionization balance, in addition to requiring the independence of the Fe line abundances with the EWs. Such a methodology has the advantage of directly estimating the microturbulent velocity, which is a needed parameter for an abundance analysis, and being independent of fitting for the projected rotation velocity (v sin$i$), macroturbulent velocity and the instrumental profile.

The limited wavelength coverage of the Hydra spectra combined with a resolving power ($R = \lambda/\Delta\lambda = 18{,}500$) that is

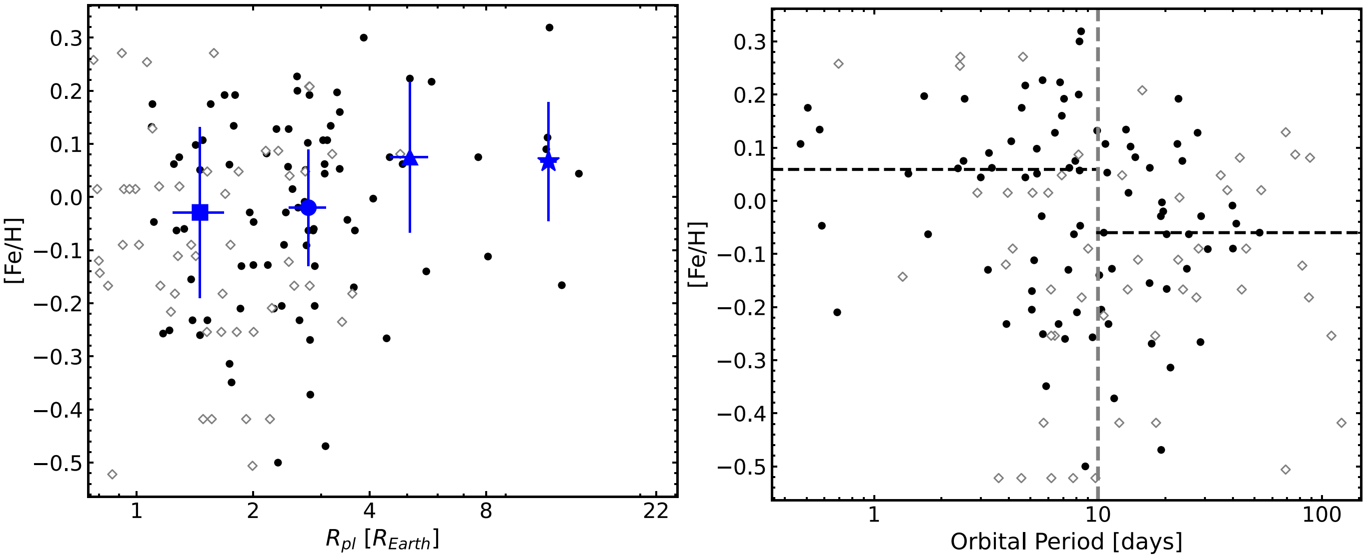

Figure 17. Host-star metallicities as a function of the planetary radius (left panel) and orbital period (right panel). K2 planets are shown as black filled circles and Kepler 1 planets as open diamonds. Left panel: the blue symbols are the median host-star metallicities for super-Earths (square), sub-Neptunes (circle), sub-Saturns (triangle), and Jupiters (star). Right panel: the horizontal dashed lines are the median host-star metallicities for planets having orbital periods smaller and larger than 10 days.

lower than that typically found in single-object high-resolution spectrographs, demanded a systematic and careful selection of unblended Fe I and Fe II lines combined with a “boutique” analysis of a benchmark solar twin to assess the reliability of the individual line results. The methodology and line list were then validated via the analysis of two solar-proxy spectra (obtained with the Hydra spectrograph) of the asteroids Astraea and Parthenope, which resulted in effective temperatures, surface gravity values, and metallicities that are similar to cannonical values in the literature for the Sun (Asplund et al. 2021; Magg et al. 2022).

Once the line list was vetted, the spectral analysis was done semiautomatically using the code q^2 (Ramirez et al. 2014) that interpolates atmospheric models, computes iron abundances, and their corresponding errors. Additional stellar properties, such as stellar masses and radii, were also computed using the q^2 package, where the input parameters were the derived effective temperatures and metallicities, along with V magnitudes, parallaxes from Gaia EDR3, and their corresponding uncertainties and isochrones from Yonsei–Yale (Demarque et al. 2004; Han et al. 2009)

The analyzed K2 stellar sample has distributions of effective temperature, surface gravity, and metallicity that fall mostly between $T_{\rm eff} \sim 4800$–6200 K, log $g \sim 3.7$–4.6, and [Fe/H] ∼−0.5 − 0.3 dex, respectively. These stars all have distances (Bailer-Jones et al. 2021) within ∼900 pc of the Sun, with most of them having stellar radii between 1 and 2 $R_\odot$, and only a few stars having radii between 2 and 4 $R_\odot$; their masses vary mostly between $\sim M_{\rm star} = 0.7$–$1.2\ M_\odot$.

Stellar radii and transit depth values are needed to constrain planetary radii, which is a crucial parameter necessary to unveil planetary composition. Most of the transit depth values for K2 planets here were from Kruse et al. (2019), and the internal precision achieved in the derived planetary radii in this work is 4.44%.

The results derived here for $T_{\rm eff}$, log g, A(Fe), $R_{\rm star}$, $M_{\rm star}$, and $R_{\rm pl}$ were compared to, and found to be in general agreement with, results obtained in several literature studies that were based on high-resolution spectra and asteroseismology for Kepler 1 stars, as well as results obtained through photometry, spectrum synthesis, and asteroseismology for K2 stars. More specifically, comparisons between our results and those in spectroscopic studies and surveys for both $T_{\rm eff}$ and log g, find agreement within ∼100 K and <0.1 dex, respectively. A closer inspection reveals consistent offsets in the sense that the effective temperatures derived here are hotter and the surface gravities slightly lower, with median differences taken over all studies (“Other Work–This Work”) of $\langle \Delta T_{\rm eff} \rangle = -37 \pm 38$ K and $\langle \Delta \log g \rangle = 0.05 \pm 0.04$ dex.

The possible impact that magnetic stellar activity might have on the derived stellar parameters was investigated by removing Fe I lines that were found to be the most sensitive to Zeeman broadening/enhancement. A subset of 15 stars that were deemed likely to be active were reanalyzed using these less magnetically sensitive Fe I lines. No significant differences, beyond the expected uncertainties, were found between the results from an analysis that included magnetically sensitive lines when compared to the analysis which excluded such lines. Based on this exercise, we do not find evidence that the stellar parameters presented here have been biased significantly by underlying stellar activity.

The relations between planet radius and orbital period and metallicity in our small K2 planet sample confirm previous results in the literature for Kepler 1 planets (Mulders et al. 2016; Petigura et al. 2018b; Narang et al. 2018; Wilson et al. 2018; Ghezzi et al. 2021). Overall, the metallicity of K2 planet hosts increases with planetary radius; this increase in metallicity is seen in particular for the transition between the small (<4.4 $R_\oplus$) and large (>4.4 $R_\oplus$) planet regimes. The median K2 host-star metallicity for planets with orbital periods < 10 days is slightly metal-rich, while the median host-star metallicity for planets with P > 10 days is slightly metal-poor. When we restrict the sample to that having only planets with $R_{\rm pl} < 4.4\ R_\oplus$, we obtain a similar behavior.

Previous studies deriving precise values for planetary radii (Fulton et al. 2017; Petigura et al. 2017; Van Eylen et al. 2018; Martinez et al. 2019) have uncovered signatures, such as the radius gap, and the slope in the radius gap with orbital period, which would not be apparent when uncertainties in stellar parameters are higher. The distribution of K2 planetary radii resulting from the stellar parameters derived here reveals a well-defined radius gap, with a minimum at $R_{\rm pl} \sim 1.9\ R_\oplus$. This gap falls at the same radius value as found for planets orbiting stars found by Kepler 1; the similarity between differing samples of exoplanet-hosting stars inhabiting larger swathes of volume across the galaxy points to the radius gap as a common feature of short-period ($P < 100$ days) exoplanetary systems. Such a conclusion concerning K2 planetary radii was also reached by Zink et al. (2020).

Although the number of K2 planetary radii derived here is relatively small, the radius gap as a function of orbital period defined by this sample is in agreement with the decreasing value of $R_{\rm pl}$ with increasing orbital period (P) found in previous studies of Kepler 1 planets (e.g., Van Eylen et al. 2018; Martinez et al. 2019), where the minimum of the radius gap follows a trend of $R_{\rm gap} \propto P^{-0.11}$.

This study adds to the list of K2 hosts with stellar parameters from high-resolution spectra, which is crucial for the field of exoplanet studies.

We thank the referee for detailed comments that helped improve the paper. We thank Ivan Ramirez for his support regarding the use and handling of the `qoyllur-quipu` code. V.L-T. acknowledges the financial support from Coordenação de Aperfeiçoamento de Pessoal de Nível Superior (CAPES). S. C.S was supported by David Delo Research Professor and Dana Foundation grants from the University of Tampa. This work is based on observations at Kitt Peak National Observatory at NSF's NOIRLab (NOIRLab Prop. ID 2019A-0334; PI: V. Smith), which is managed by the Association of Universities for Research in Astronomy (AURA) under a cooperative agreement with the National Science Foundation. The authors are honored to be permitted to conduct astronomical research on Iolkam Du'ag (Kitt Peak), a mountain with particular significance to the Tohono O'odham. Data presented were obtained at the WIYN Observatory, operated by NOIRLab, under the NN-EXPLORE partnership of the National Aeronautics and Space Administration and the National Science Foundation. This work was supported by a NASA WIYN PI Data Award, administered by the NASA Exoplanet Science Institute. This research has made use of the NASA Exoplanet Archive, which is operated by the California Institute of Technology, under contract with NASA under the Exoplanet Exploration Program. K.C. and V.S. acknowledge that their work here is supported, in part, by the National Science Foundation through NSF grant No. AST-2009507.

ORCID iDs

V. Loaiza-Tacuri https://orcid.org/0000-0003-0506-8269
Katia Cunha https://orcid.org/0000-0001-6476-0576
Verne V. Smith https://orcid.org/0000-0002-0134-2024
Luan Ghezzi https://orcid.org/0000-0002-9089-0136
Simon C. Schuler https://orcid.org/0000-0001-7203-8014
Steve B. Howell https://orcid.org/0000-0002-2532-2853

References

Adibekyan, V. 2019, Geosc, 9, 105
Adibekyan, V., Santos, N. C., Figueira, P., et al. 2015, A&A, 581, L2
Adibekyan, V. Z., Figueira, P., Santos, N. C., et al. 2013, A&A, 560, A51
Armstrong, D. J., Kirk, J., Lam, K. W. F., et al. 2015, A&A, 579, A19
Asplund, M., Amarsi, A. M., & Grevesse, N. 2021, A&A, 653, A141
Aguirre, V. S., Lund, M. N., Antia, H. M., et al. 2017, ApJ, 835, 173
Bailer-Jones, C. A. L., Rybizki, J., Fouesneau, M., Demleitner, M., & Andrae, R. 2021, AJ, 161, 147
Bailer-Jones, C. A. L., Rybizki, J., Fouesneau, M., Mantelet, G., & Andrae, R. 2018, AJ, 156, 58
Bard, A., & Kock, M. 1994, A&A, 282, 1014
Barros, S. C. C., Demangeon, O., & Deleuil, M. 2016, A&A, 594, A100
Batalha, N. M., Rowe, J. F., Bryson, S. T., et al. 2013, ApJS, 204, 24
Beauge, C., & Nesvorny, D. 2013, ApJ, 763, 12
Bensby, T., Feltzing, S., & Oey, M. S. 2014, A&A, 562, A71
Berger, T. A., Huber, D., Gaidos, E., & van Saders, J. L. 2018, ApJ, 866, 99
Berger, T. A., Huber, D., Gaidos, E., van Saders, J. L., & Weiss, L. M. 2020a, AJ, 160, 108
Berger, T. A., Huber, D., van Saders, J. L., et al. 2020b, AJ, 159, 280
Borucki, W. J. 2016, RPPh, 79, 036901
Borucki, W. J., Koch, D., Basri, G., et al. 2010, Sci, 327, 977
Boyajian, T. S., von Braun, K., van Belle, G., et al. 2013, ApJ, 771, 40
Brewer, J. M., & Fischer, D. A. 2018, ApJS, 237, 38
Brewer, J. M., Fischer, D. A., Valenti, J. A., & Piskunov, N. 2016, ApJS, 225, 32
Brown, E. L., Jeffers, S. V., Marsden, S. C., et al. 2022, MNRAS, 514, 4300
Buchhave, L. A., Bizzarro, M., Latham, D. W., et al. 2014, Natur, 509, 593
Buchhave, L. A., & Latham, D. W. 2015, ApJ, 808, 187
Buchhave, L. A., Latham, D. W., Johansen, A., et al. 2012, Natur, 486, 375
Buder, S., Sharma, S., Kos, J., et al. 2021, MNRAS, 506, 150
Castelli, F., & Kurucz, R. L. 2003, in IAU Symp. 210, Modelling of Stellar Atmospheres, ed. N. Piskunov, W. W. Weiss, & D. F. Gray (San Francisco, CA: ASP), A20
Choi, J., Dotter, A., Conroy, C., et al. 2016, ApJ, 823, 102
Clark, J. T., Wright, D. J., Wittenmyer, R. A., et al. 2022, MNRAS, 510, 2041
Cloutier, R., & Menou, K. 2020, AJ, 159, 211
Crossfield, I. J. M., Ciardi, D. R., Petigura, E. A., et al. 2016, ApJS, 226, 7
Crossfield, I. J. M., Guerrero, N., David, T., et al. 2018, ApJS, 239, 5
Cui, X.-Q., Zhao, Y.-H., Chu, Y.-Q., et al. 2012, RAA, 12, 1197
da Silva, L., Girardi, L., Pasquini, L., et al. 2006, A&A, 458, 609
Damasso, M., Zeng, L., Malavolta, L., et al. 2019, A&A, 624, A38
Dawson, R. I., Chiang, E., & Lee, E. J. 2015, MNRAS, 453, 1471
Deleuil, M., Barge, P., Defay, C., et al. 2000, in ASP Conf. Ser. 219, Disks, Planetesimals, and Planets, ed. C. Garzón et al. (San Francisco, CA: ASP), 656
Deleuil, M., Aigrain, S., Moutou, C., et al. 2018, A&A, 619, A97
Demarque, P., Woo, J.-H., Kim, Y.-C., & Yi, S. K. 2004, ApJS, 155, 667
Dong, S., Xie, J.-W., Zhou, J.-L., Zheng, Z., & Luo, A. 2018, PNAS, 115, 266
Dotter, A. 2016, ApJS, 222, 8
Dotter, A., Chaboyer, B., Jevremovic, D., et al. 2008, ApJS, 178, 89
Epstein, C. R., Johnson, J. A., Dong, S., et al. 2010, ApJ, 709, 447
Everett, M. E., Howell, S. B., Silva, D. R., & Szkody, P. 2013, ApJ, 771, 107
Fischer, D. A., & Valenti, J. 2005, ApJ, 622, 1102
Flores, M., Gonzalez, J. F., Jaque Arancibia, M., Buccino, A., & Saffe, C. 2016, A&A, 589, A135
Friel, E. D., Jacobson, H. R., Barrett, E., et al. 2003, AJ, 126, 2372
Fulton, B. J., & Petigura, E. A. 2018, AJ, 156, 264
Fulton, B. J., Petigura, E. A., Howard, A. W., et al. 2017, AJ, 154, 109
Furlan, E., & Howell, S. B. 2017, AJ, 154, 66
Furlan, E., Ciardi, D. R., Everett, M. E., et al. 2017, AJ, 153, 71
Gaia Collaboration, Brown, A. G. A., Vallenari, A., et al. 2021, A&A, 649, A1
Gaudi, B. S. 2013, AAS Meeting, 221, 310.03
Ghezzi, L., Cunha, K., Schuler, S. C., & Smith, V. V. 2010, ApJ, 725, 721
Ghezzi, L., Martinez, C. F., Wilson, R. F., et al. 2021, ApJ, 920, 19
Ghezzi, L., Montet, B. T., & Johnson, J. A. 2018, ApJ, 860, 109
Ginzburg, S., Schlichting, H. E., & Sari, R. 2016, ApJ, 825, 29
Ginzburg, S., Schlichting, H. E., & Sari, R. 2018, MNRAS, 476, 759
Girardi, L., Bressan, A., Bertelli, G., & Chiosi, C. 2000, A&AS, 141, 371
Gonzalez, G. 1997, MNRAS, 285, 403
Gupta, A., & Schlichting, H. E. 2019, MNRAS, 487, 24
Han, S. I., Kim, Y. C., Lee, Y. W., et al. 2009, Globular Clusters—Guides to Galaxies. Eso Astrophysics Symp., ed. T. Richter & S. Larsen (Berlin: Springer), 33
Hardegree-Ullman, K. K., Zink, J. K., Christiansen, J. L., et al. 2020, ApJS, 247, 28
Hayden, M. R., Bovy, J., Holtzman, J. A., et al. 2015, ApJ, 808, 132
Hayden, M. R., Bland-Hawthorn, J., Sharma, S., et al. 2020, MNRAS, 493, 2952
Howell, S. B., Matson, R. A., Ciardi, D. R., et al. 2021, AJ, 161, 164
Howell, S. B., Sobeck, C., Haas, M., et al. 2014, PASP, 126, 398

Huber, D., Bryson, S. T., Haas, M. R., et al. 2016, ApJS, 224, 2
Huber, D., Zinn, J., Bojsen-Hansen, M., et al. 2017, ApJ, 844, 102
Ida, S., & Lin, D. N. C. 2004a, ApJ, 604, 388
Ida, S., & Lin, D. N. C. 2004b, ApJ, 616, 567
Ida, S., & Lin, D. N. C. 2005, ApJ, 626, 1045
Johnson, J. A., Petigura, E. A., Fulton, B. J., et al. 2017, AJ, 154, 108
Jonsson, H., Holtzman, J. A., Prieto, C. A., et al. 2020, AJ, 160, 120
Koch, D. G., Borucki, W. J., Basri, G., et al. 2010, ApJL, 713, L79
Kruse, E., Agol, E., Luger, R., & Foreman-Mackey, D. 2019, ApJS, 244, 11
Kurucz, R. L. 2014, in Determination of Atmospheric Parameters of B-, A-, F- and G-Type Stars, ed. E. Niemczura, B. Smalley, & W. Pych (Berlin: Springer), 63
LaCourse, D. M., Jek, K. J., Jacobs, T. L., et al. 2015, MNRAS, 452, 3561
Lester, K. V., Matson, R. A., Howell, S. B., et al. 2021, AJ, 162, 75
Libralato, M., Nardiello, D., Bedin, L. R., et al. 2016, MNRAS, 463, 1780
Livingston, J. H., Crossfield, I. J. M., Petigura, E. A., et al. 2018, AJ, 156, 277
Lopez, E. D., & Fortney, J. J. 2013, ApJ, 776, 2
Lorenzo-Oliveira, D., Freitas, F. C., Melendez, J., et al. 2018, A&A, 619, A73
Magg, E., Bergemann, M., Serenelli, A., et al. 2022, A&A, 661, A140
Majewski, S. R., Schiavon, R. P., Frinchaboy, P. M., et al. 2017, AJ, 154, 94
Mann, A. W., Gaidos, E., Vanderburg, A., et al. 2017, AJ, 153, 64
Martin, E. L., Lodieu, N., Pavlenko, Y., & Bejar, V. J. S. 2018, ApJ, 856, 40
Martinez, C. F., Cunha, K., Ghezzi, L., & Smith, V. V. 2019, ApJ, 875, 29
Mayo, A. W., Vanderburg, A., Latham, D. W., et al. 2018, AJ, 155, 136
Meléndez, J., Ramírez, I., Karakas, A. a. I., et al. 2014, ApJ, 791, 14
Montet, B. T., Morton, T. D., Foreman-Mackey, D., et al. 2015, ApJ, 809, 25
Mordasini, C., Alibert, Y., Benz, W., Klahr, H., & Henning, T. 2012, A&A, 541, A97
Mordasini, C., Molliere, P., Dittkrist, K.-M., Jin, S., & Alibert, Y. 2015, IJAsB, 14, 201
Morton, T. D. 2015, isochrones: Stellar model grid package, Astrophysics Source Code Library, ascl:1503.010
Mulders, G. D., Pascucci, I., Apai, D., Frasca, A., & Molenda-Zakowicz, J. 2016, AJ, 152, 187
Mullally, F., Coughlin, J. L., Thompson, S. E., et al. 2015, ApJS, 217, 31
Narang, M., Manoj, P., Furlan, E., et al. 2018, AJ, 156, 221
Nayakshin, S. 2010, MNRAS, 408, L36
Oláh, Katalin 2007, in IAU Symp. 240, Binary Stars as Critical Tools & Tests in Contemporary Astrophysics, ed. W. I. Hartkopf, P. Harmanec, & E. F. Guinan (Cambridge: Cambridge Univ. Press), 442
Owen, J. E., & Murray-Clay, R. 2018, MNRAS, 480, 2206
Owen, J. E., & Wu, Y. 2013, ApJ, 775, 105
Petigura, E. A., Crossfield, I. J. M., Isaacson, H., et al. 2018a, AJ, 155, 21
Petigura, E. A., Howard, A. W., Marcy, G. W., et al. 2017, AJ, 154, 107
Petigura, E. A., Marcy, G. W., Winn, J. N., et al. 2018b, AJ, 155, 89
Petigura, E. A., Rogers, J. G., Isaacson, H., et al. 2022, AJ, 163, 179
Pinsonneault, M. H., Elsworth, Y. P., Tayar, J., et al. 2018, ApJS, 239, 32
Piskunov, N., & Valenti, J. A. 2017, A&A, 597, A16
Pope, B. J. S., Parviainen, H., & Aigrain, S. 2016, MNRAS, 461, 3399
Ramirez, I., Allende Prieto, C., & Lambert, D. L. 2013, ApJ, 764, 78
Ramirez, I., Melendez, J., & Asplund, M. 2009, A&A, 508, L17
Ramirez, I., Melendez, J., Bean, J., et al. 2014, A&A, 572, A48
Ricker, G. R., Winn, J. N., Vanderspek, R., et al. 2015, JATIS, 1, 014003
Rizzuto, A. C., Mann, A. W., Vanderburg, A., Kraus, A. L., & Covey, K. R. 2017, AJ, 154, 224
Rodrigues, T. S., Bossini, D., Miglio, A., et al. 2017, MNRAS, 467, 1433
Rodrigues, T. S., Girardi, L., Miglio, A., et al. 2014, MNRAS, 445, 2758
Santos, N. C., Israelian, G., & Mayor, M. 2004, A&A, 415, 1153
Schuler, S. C., Vaz, Z. A., Katime Santrich, O. o. J., et al. 2015, ApJ, 815, 5
Seager, S., & Mallen-Ornelas, G. 2003, ApJ, 585, 1038
Serenelli, A., Johnson, J., Huber, D., et al. 2017, ApJS, 233, 23
Sharma, S., Stello, D., Bland-Hawthorn, J., et al. 2019, MNRAS, 490, 5335
Sinukoff, E., Howard, A. W., Petigura, E. A., et al. 2016, ApJ, 827, 78
Slawson, R. W., Prsa, A., Welsh, W. F., et al. 2011, AJ, 142, 160
Sneden, C. A. 1973, PhD thesis, The University of Texas at Austin
Sousa, S. G., Santos, N. C., Adibekyan, V., Delgado-Mena, E., & Israelian, G. 2015, A&A, 577, A67
Sousa, S. G., Santos, N. C., Israelian, G., Mayor, M., & Udry, S. 2011, A&A, 533, A141
Sousa, S. G., Santos, N. C., Mayor, M., et al. 2008, yCat, 348, 70373
Spina, L., Nordlander, T., Casey, A. R., et al. 2020, ApJ, 895, 52
Stassun, K. G., Oelkers, R. J., Paegert, M., et al. 2019, AJ, 158, 138
Stefansson, G., Li, Y., Mahadevan, S., et al. 2018, AJ, 156, 266
Su, T., Zhang, L.-y., Long, L., et al. 2022, ApJS, 261, 26
Thompson, S. E., Coughlin, J. L., Hoffman, K., et al. 2018, ApJS, 235, 38
van Dokkum, P. G. 2001, PASP, 113, 1420
Van Eylen, V., Agentoft, C., Lundkvist, M. S., et al. 2018, MNRAS, 479, 4786
Van Eylen, V., Albrecht, S., Gandolfi, D., et al. 2016, AJ, 152, 143
Van Eylen, V., Astudillo-Defru, N., Bonfils, X., et al. 2021, MNRAS, 507, 2154
Vanderburg, A., Latham, D. W., Buchhave, L. A., et al. 2016, ApJS, 222, 14
Venturini, J., Guilera, O. M., Haldemann, J., Ronco, M. P., & Mordasini, C. 2020, A&A, 643, L1
Wang, J., & Fischer, D. A. 2015, AJ, 149, 14
Weiss, L. M., Isaacson, H. T., Marcy, G. W., et al. 2018, AJ, 156, 254
Wilson, R. F., Teske, J., Majewski, S. R., et al. 2018, AJ, 155, 68
Wittenmyer, R. A., Sharma, S., Stello, D., et al. 2018, AJ, 155, 84
Wittenmyer, R. A., Clark, J. T., Sharma, S., et al. 2020, MNRAS, 496, 851
Yana Galarza, J., Meléndez, J., Lorenzo-Oliveira, D., et al. 2019, MNRAS, 490, L86
Yi, S., Demarque, P., Kim, Y.-C., et al. 2001, ApJS, 136, 417
Yi, S. K., Kim, Y.-C., & Demarque, P. 2003, ApJS, 144, 259
Zhu, W., Wang, J., & Huang, C. 2016, ApJ, 832, 196
Zink, J. K., Hardegree-Ullman, K. K., Christiansen, J. L., et al. 2020, AJ, 160, 94
Zink, J. K., Hardegree-Ullman, K. K., Christiansen, J. L., et al. 2021, AJ, 162, 259
Zong, W., Fu, J.-N., Cat, P. D., et al. 2018, ApJS, 238, 30